

Methods for modeling and predicting mechanical deformations of the breast under external perturbations

Fred S. Azar^{a,*}, Dimitris N. Metaxas^b, Mitchell D. Schnall^c

^aDepartment of BioEngineering, University of Pennsylvania, 120 Hayden Hall, 3320 Smith Walk, Philadelphia, PA 19104, USA

^bDepartment of Computer Science, University of Pennsylvania, 200 South 33rd St., Philadelphia, PA 19104, USA

^cDepartment of Radiology, Hospital of the University of Pennsylvania, MRI Bldg. 1 Founders, 3400 Spruce St., Philadelphia, PA 19104, USA

Received 18 May 2001; accepted 31 August 2001

Abstract

Currently, high field (1.5 T) superconducting MR imaging does not allow live guidance during needle breast procedures. The current procedure allows the physician only to calculate approximately the location and extent of a cancerous tumor in the compressed patient breast before inserting the needle. It can then become relatively uncertain that the tissue specimen removed during the biopsy actually belongs to the lesion of interest. A new method for guiding clinical breast biopsy is presented, based on a deformable finite element model of the breast. The geometry of the model is constructed from MR data, and its mechanical properties are modeled using a non-linear material model. This method allows imaging the breast without or with mild compression before the procedure, then compressing the breast and using the finite element model to predict the tumor's position during the procedure. A silicon phantom containing a stiff inclusion was imaged uncompressed then compressed. A model of the phantom was constructed and compressed using custom-written software, and also using a commercial FEM simulation package. The displacement of the inclusion's corners was recorded both in the real phantom and in the two compressed models. A patient's breast was imaged uncompressed then compressed. A deformable model of the uncompressed breast was constructed, then compressed. The displacement of a cyst and of two vitamin E pills taped to the surface of the breast were recorded both in the real and in the modeled breast. The entire procedure lasted less than a half-hour, making it clinically useful. The results show that it is possible to create a deformable model of the breast based on finite elements with non-linear material properties, capable of modeling and predicting breast deformations in a clinically useful amount of time. © 2002 Elsevier Science B.V. All rights reserved.

Keywords: MRI; Finite element modeling; Breast cancer; Soft tissue modeling

1. Introduction

The ability to identify a mass in the breast requires that the mass has a different appearance (or a different contrast) from normal tissue. With MRI, the contrast between soft tissues in the breast is 10–100 times greater than that obtained with X-rays (Fischer et al., 1994, 1995; Orel et al., 1994). A MR image-guided breast localization and biopsy system is needed to help differentiate between the benign enhancing lesions, and carcinomas (Orel et al.,

1994). A whole-body MR system at 1.5 T (Signa; GE Medical Systems, Milwaukee, WI) is used for all needle localizations. The technique requires that the patient lies prone with the breast gently compressed between medial and lateral plates. A multicoil array is used, with two coils placed on the medial plate and one coil on the lateral plate. The lateral plate contains a grid of approximately 1000 18-gauge holes placed at 5-mm intervals, which guide the needle in a plane parallel to the tabletop. The correct hole in the plate is identified and a needle is inserted through that hole into the breast with a pre-calculated depth. However the MR imaging-guided localization technique encounters the following problems:

- The appearance, size and shape of the potential cancer

*Corresponding author. 2231 Kaitlyn Court, West Windsor, NJ 08550, USA. Tel.: +1-609-750-0565.

E-mail address: fredazar@graphics.cis.upenn.edu (F.S. Azar).

lesion greatly depend on the dynamics of the contrast-enhancing agent. The lesion may clearly appear only in the 2 minutes following the contrast agent injection, then the signal intensity may vary arbitrarily, and it is possible that the apparent boundaries of the lesion may change dramatically.

- The needle is not a very sharp object, and cannot be smoothly inserted in the breast. Every time the tip of the needle reaches the interface between two different types of tissue, its further insertion will push the tissue instead of piercing it, causing unwanted deformations until the pressure on the tissue interface is high enough. As soon as the needle pierces the displaced tissue interface, that interface quickly settles back to its original position, or somewhere close to it. The best way to remedy this problem would be to compress the breast as much as possible, which would minimize internal deformations. However doing that would cause blood to be squeezed out of the breast, and would dramatically alter the appearance and shape of the lesion on the MR image, without mentioning the high level of discomfort for the patient who would be very reluctant to feel the pain for the entire duration of the procedure. The best solution would be to mildly compress the breast and obtain MR images clearly showing the position, shape and extent of the lesion. Then the breast would be highly compressed in order to minimize internal deformations during the needle insertion only. However the missing link is to predict the displacement of the lesion from the mildly compressed configuration, to the highly compressed configuration.

The above limitations coupled with the deformable structure of the breast makes needle procedures very sensitive to the initial placement of the needle, and to the amount of breast compression. It thus becomes relatively uncertain that the tissue specimen removed during the biopsy procedure actually belongs to the lesion of interest, due to the added difficulty of accurately locating the tumor's boundaries inside the breast. It is therefore important to develop techniques, which would solve or bypass the aforementioned problems, increase the level of confidence of a biopsy result (improving the diagnosis), and decrease the cost to society (including health care expenses). The financial savings could be considerable, and the morbidity associated with the biopsy procedure including the lost time from work that occurs as a result of biopsy could be greatly reduced (Stavros et al., 1995).

We present a virtual deformable breast model of the patient whose geometry is constructed from MR data. The elastic properties of the deformable model are based on the use of finite elements with nonlinear material properties capable of modeling the deformation of the breast under external perturbations. A high-field 1.5-Tesla machine Signa Horizon Echospeed (GEMS, Milwaukee, WI) is used to obtain the 3D breast image sets. The image sets are used to construct the geometry of the finite element model. Contours of the breast are extracted, and each breast slice

is segmented to locate the different tissue types, using appropriate custom-written software. The model geometry is then created using a custom-written preprocessor, which allows for a variable mesh size. We also developed a software algorithm (*BreastView*), which models large deformations of the breast model depending on the desired accuracy of the deformation. We hypothesize that the structural complexity of the breast can be simplified to only assign to the model elements, an average value of the mechanical properties of glandular, fatty, and cancerous tissue.

The major novelties in this model include the following:

- Breast plate compression plates results in a large compression, meaning that the total distance between the two plates decreases by more than 10%. In order to model such large deformations, we divide the large deformation compression into a number of much smaller displacement steps. For every displacement step, we make use of small strain theory. Strain is calculated using Cauchy's infinitesimal strain tensor formula (Fung, 1994). After every small displacement iteration, the tissues's different material properties are recalculated in all model elements whose maximum principal strain has changed, in order to model the materials' non-linear behavior. The main advantage of using small strain formulation lies in its simplicity, ease of implementation and fast computation. However, being an incremental formulation, it could lead to an accumulation of discretization errors and in consequence, to a lack of accuracy (Szekely et al., 1998). A way to solve this potential problem would be to use a total Lagrange formulation (as the one we use for estimating the non-linear material properties of tissue from one displacement iteration to the next), in which every state is related to the initial configuration. However that would complicate the formulation and slow down the computation of the solution. We show in a silicon phantom study that the incremental errors introduced by small strain formulation can be neglected for the purpose of this model and overall study.
- We present a new breast fatty tissue material model, which takes into account the effect of fat compartmentalization due to Cooper's ligaments in the breast. We show through empirical evidence that fat compartmentalization occurs as the breast is being compressed, and that the new updated fatty tissue material model takes that phenomenon into account, and performs better than the original fatty tissue model.
- We apply finite element modeling theory to model the deformation of a human female breast in such a way that the entire process takes less than a half-hour (compared to several hours using a commercial finite element modeling package), which according to the clinicians consulted, is a reasonably short time duration.

This model can be used effectively in several different applications:

- *A new method for guiding clinical breast biopsy:* This

method involves imaging the patient's breast without any or little compression before a needle procedure, then compressing the breast, and its virtual finite element model (by applying the same pressure to both), and using the displacement of the virtual tumor model to predict the displacement of the real cancer tumor. It is important to note that during the entire procedure (imaging, needle localization, and/or biopsy), the patient remains in the same prone position, and only the equipment 'moves' around the patient. Therefore perturbations caused by the patient's movements are minor. A model like the one presented here is important to this procedure, in which any improvement in confidence for localizing the cancer tumor could become life-saving.

- *Other applications:* A finite element model of the breast can be a very flexible tool for many applications including registration of different breast MR data sets of the same patient taken under different compression amounts, or registration of different data sets from different imaging modalities. Other possible applications include diagnosis, measurements, surgery planning, simulations of deformation due to inserting a needle, and further away, virtual surgery, and tele-surgery.

The paper is organized as follows.

1. In Section 2, the related work is presented and compared to our model. The general flowchart of operation is described.
2. Section 3 presents the methods used, going through image acquisition, data extraction, 3D mesh domain creation, model dynamics, and the description of the internal forces due to stiffness.
3. Section 4 presents the experimental methods:
 - (a) A deformable silicon gel phantom was built to study the movement of a stiff inclusion inside a deformable environment under plate compression. The phantom was imaged undeformed, then compressed (14%). The performance of our software algorithm was compared to that of a robust commercial FEM software package. A 3D deformable model of the phantom was built from the resulting MR data using our custom-written software and was virtually compressed using *BreastView*. Another FEM was built using a commercial pre-processor (PATRAN, MSC, CA) from the phantom's directly measured dimensions, and was virtually compressed using ABAQUS (HKS, RI). The displacement vectors of the 8 corners of the stiff inclusion and its center were measured both from the MR images and from the two finite element models.
 - (b) A patient's breast was imaged uncompressed and then compressed 26%. The corresponding deformable model was built, and was virtually compressed to match the real compression amount. We tracked the displacement of a small cyst inside the patient's breast, and used the deformable model to predict the

cyst's position in the real compressed breast. We also tracked the displacement of two vitamin E pills taped to the surface of the patient's breast.

4. Section 5 presents the results and discussion for both experiments. We also present a convergence analysis, and a material properties sensitivity analysis. The results show that it is possible to create a deformable model of the breast based on the use of finite elements with non-linear material properties, capable of modeling the deformation of the breast in a clinically useful amount of time (less than a half-hour for the entire procedure).
5. Section 6 deals with additional issues, including the potential sources of error, specific properties of reliability, and summarizes the major novelties in the model.
6. Section 7 presents the concluding remarks, and is followed by Appendices A–C which present the finite element modeling theory in detail, as well as details of the silicon phantom construction.

2. Related work

Finite element modeling has been used in a very large number of fields. However, it is only recently that deformable models have been used to simulate deformations in soft tissue. Physical models are among the first to be used. Among these physical models, elastic (linear and visco-elastic) models have been extensively described in the literature (Chen and Zeltzer, 1992; Speeter, 1992; Reddy and Song, 1995). The most widely used representations for deformable volumes are parametric models with B-spline representation (Zienkiewicz, 1977). Other possible models are mass-spring models (Miller, 1988; Chadwick et al., 1989; Luciani et al., 1991; Norton et al., 1991; Joukhadar, 1995), and implicit surfaces (Desbrun and Gascuel, 1995). The mass-spring methods have been used most of the time for surgery simulation due to their simplicity of implementation and their lower computational complexity (Kuehnappel and Neisius, 1993; Baumann and Glauser, 1996; Meseure and Chaillou, 1997). Other methods have relied on geometry rather than physics to predict breast deformation (Behrenbruch et al., 2000).

Finite element models are less widely used due to the difficulty of their implementation and their larger computing time. There are many powerful commercial FEM packages that allow complex simulations of deformation such as ABAQUS (HKS); breast tissue is relatively complex, and consists of layers of different tissues interlaced with ligaments and fascias. Very complex models would be needed to model these objects realistically. However the complexity of the model and the required computational time (which can extend to several days on a SGI workstation) would prohibit these models from being useful clinically. Few models of the breast have actually been implemented using the commercial software pack-

ages, and have mostly involved phantom studies (Azar et al., 1999; Sciaretta et al., 1999; Williams et al., 1999). A real-time system has been recently developed for hepatic surgery simulation, and involves deformations of soft tissue (Cotin et al., 1999). An explicit large displacement model for interactive surgery simulation using fast non-linear finite element models was also proposed by Picinbono et al. (2001), and models for physically realistic simulation of global deformation were proposed by Zhuang and Canny (1999).

The desired accuracy of the deformation in the breast model must therefore be balanced against the need for speed. In order to develop a model for deformation of the breast, we must decide on a geometric description of the breast, a mathematical model of the elastic deformation, and a solution algorithm that is both fast and yields a reasonably realistic result. For that reason, what matters most is that the breast deformation results be realistic and available in a clinically useful time (less than 30 minutes for the entire procedure), and that the model be robust and show a consistent and predictable behavior. In our approach, we strive to integrate the requirements for a realistic simulation of deformation, and the reasonably fast time modeling which is a necessity if the model is to be

used in a clinical environment: by incorporating the geometric definition of the breast model into the physics-based framework developed in (Metaxas, 1992; Metaxas and Terzopoulos, 1993), we create a deformable breast model, capable of reasonably predicting the internal deformations of a real patient breast after plate compression (Azar et al., 2001).

Fig. 1 shows the general flowchart of how the FEM of the breast is created (vertical dimension), and the process by which it is virtually compressed (horizontal dimension). We start with the patient's breast MR data which constitutes a 3D image set of parallel slices. Each of these slices is segmented and classified into different tissue types (glandular, fatty and/or cancerous) semi-automatically. Given this data, the 3D mesh of the model is generated automatically, and every element in the mesh is assigned a particular tissue type value. Then the deformation process starts from the given initial and boundary conditions. The large compression plate displacement is translated into a number of much smaller displacement iterations, each of which is applied in turn to the FEM of the breast. For each applied displacement iteration, the equation of motion must be solved and the intermediate model node displacements are calculated. Following that step, the elasticity

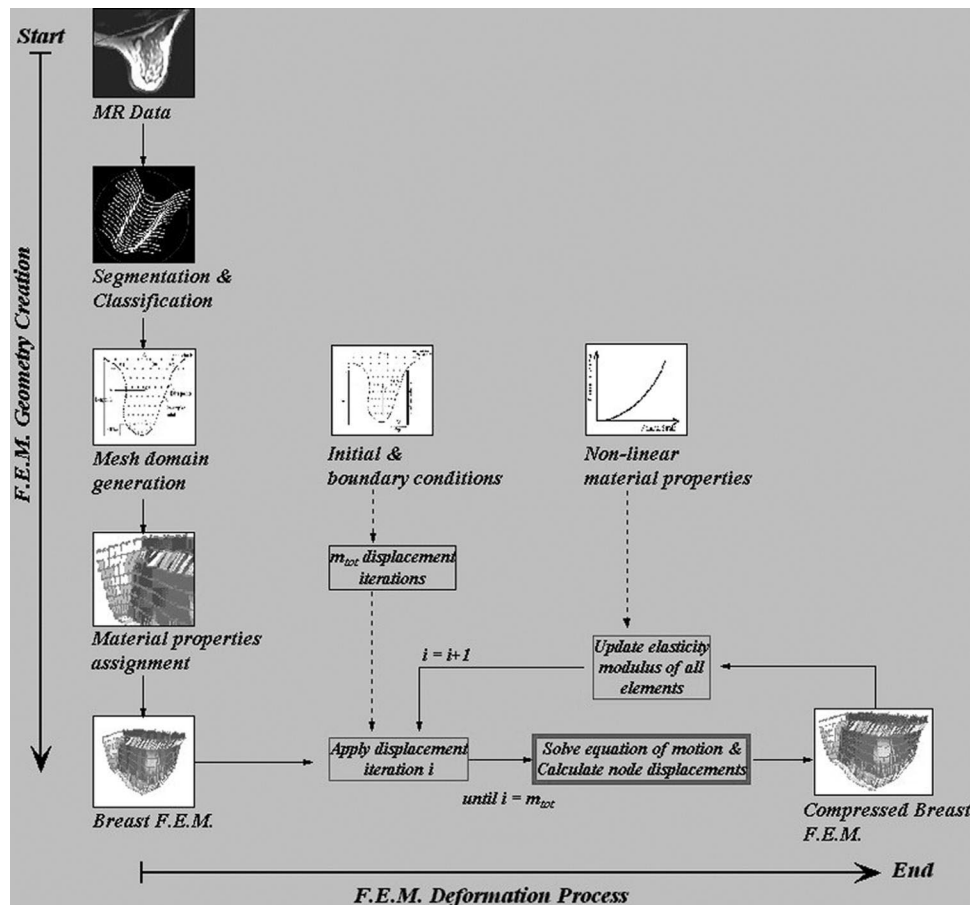


Fig. 1. General flowchart of operation.

value of every element in the model is updated given its principal strain value and the non-linear material model of the tissue type it represents. After all the displacement iterations are applied the final compressed model of the breast is obtained. Because of the high variability of breast shapes and the deformation of the breast when compressed in order to be imaged, the model devised closely follows the contours of the patient breast.

3. Methods

3.1. Image acquisition and data extraction

The patient data is a set of parallel 2D spoiled gradient echo MR axial slices of the breast. Usually, an axial T1-weighted spin echo sequence is performed with a repetition time of 500 ms, and an echo time of 12 ms, with a 12–16 cm field of view, a 1–3 mm thick section, and a 256×256 matrix. The acquisition ensures a 3D visualization of the patient's breast. First the MR image 3D set is converted into a set of axial slices (if the original data is not axial) through automatic resampling of the data using a software package such as Scion Image (Scion, MD).

The MR images are loaded to a program, which enables segmentation through contours. The contours of the breast boundary are created semi-automatically (using Scion Image and Adobe Photoshop), and saved to a file for subsequent use. At the same time each MR image is automatically segmented into parenchyma, fat and/or lesion tissue, using a robust segmentation algorithm (each tissue type is assigned a specific gray level value).

The segmentation algorithm used is based on the concept of fuzzy connectedness (Carvalho et al., 1999; Saha et al., 2000). This approach is semiautomatic, in the sense that when using the segmentation program (developed by Carvalho et al.) the user must identify seed voxels, which definitely belong to the various objects in the image (fat, glandular, cancerous tissues). The user-selected seed voxels are then used for automatic segmentation of the entire image. This algorithm yields accurate and robust results, and is able to segment a breast full MR 3D volume in less than a minute (on a standard PC workstation), after only spending a few minutes selecting the seed voxels.

3.2. 3D mesh domain creation

BreastView, a custom-written program in C, takes as input the set of breast contours and the segmentation results. Running on an SGI workstation, it generates the 3D computational domain (mesh) of the breast in a few seconds, allowing to scale the volume elements to any size. The program can also generate a finite element model (FEM) file readable by FEM software ABAQUS. This file contains the definition of the volume elements, as well as

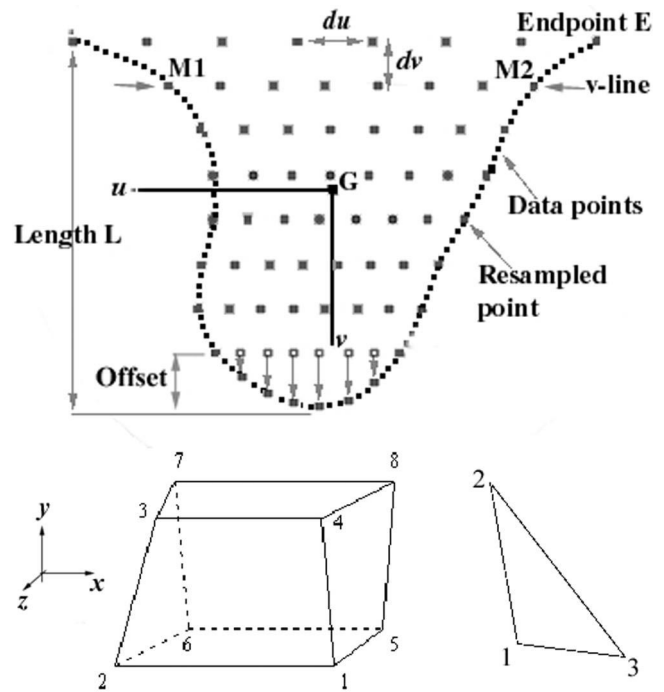


Fig. 2. Slice contour with 2D-mesh generation (top), and elements used to build the deformable model (eight-node element, three-node triangle, bottom).

the boundary conditions, and the different material properties. Two types of 3D volume elements are used in the model (Fig. 2, bottom). Solid 8-node (hexahedral) trilinear isoparametric elements are used to model all breast tissues except for the skin, and are assigned non-linear material properties. Three-node triangular isoparametric elements are used to model the skin, and are assigned non-linear elastic properties in the plane of their triangular surface, and no axial stiffness. The nodes forming the 2D mesh representing the skin are the same nodes belonging to the hexahedral elements at the borders of the breast model.

BreastView allows the mesh to be as dense as needed. These volume elements are well suited for the purpose of the model: if a physician only needs approximate information on how the tumor is moving, the tumor could be included in one volume element (by correctly scaling the mesh density) which would be assigned its own mechanical characteristics. Fig. 2(top) shows a contour and the 2D mesh generated in it.

In order to create the 3D mesh, we first find the principal direction d for the entire contour set (direction of the v -axis, Fig. 2(top)), from the chest wall to the nipple. Any line with direction d in the plane of a contour, which intersects the contour, will intersect it twice. This direction is that of the line orthogonal to the line, which passes through the two endpoints (the principal direction method using the eigenvectors of the contour set of points did not yield the best direction d). The principal direction d for the entire contour set is obtained by averaging the computed

individual slice directions. The center of gravity G of the contour set is calculated. The 3D mesh can now be easily generated following the U (along u) and V (along v) resolution desired, in the orthogonal (u, v) basis centered at G . This algorithm ensures that we have the same number of points on every V -line, and the same number of V -lines on every slice.

In order to avoid that degenerated elements at the edge of the breast may be created during the 3D meshing process, we introduce a predetermined offset for every slice, which is a percentage of the length L of the breast slice, as shown in Fig. 2. The row of element nodes generated closest to the edge of the breast slice is at a distance of $L \times \text{Offset}$ from the edge of the breast. Finally every node on this final row is projected along the v -axis onto the edge of the breast slice.

We implemented the meshing in the z -direction (number of slices) in two different ways:

- there can be as many element slices (in the z -direction) as there are segmented data slices;
- we make the meshing in the z -direction variable, increase the mesh density around the point of interest, and decrease it away from the point of interest. This scheme can enable us to decrease the total number of model slices, and hence greatly accelerate the simulation.

Since the point of interest is usually a hard inclusion such as a cyst or a tumor, it is more important for the mesh to be denser in that area than in the slices away from the inclusion, which may have less impact on the displacement of the inclusion. By implementing such an algorithm, we can also decrease the total number of model slices, thereby greatly decreasing the compression simulation time.

Once the 3D mesh is created, each element is assigned a material property corresponding to that of fat, parenchyma or cancerous tissue. In order to determine what type of material property to assign to any one 3D element, an algorithm makes use of the automatically segmented breast MR data. The algorithm calculates what percentage of fat, parenchyma and cancerous tissue lie within the element, by identifying the corresponding number of voxels which lie in the element. The material property that corresponds to the highest percentage is the one assigned to the element. It is clear from this algorithm, that the finer the mesh, and the more precise the assignment of material properties will be.

3.3. Model dynamics

The governing Lagrange equations of motion are second order differential equations given as follows (Metaxas, 1992; Metaxas and Terzopoulos, 1993):

$$M \frac{\partial^2 q}{\partial t^2} + D \frac{\partial q}{\partial t} + Kq = g_q + f_q, \quad (1)$$

where M , D and K are the mass, damping and stiffness matrices, respectively. The vector q contains the displacement degrees of freedom, g_q are the inertial forces arising from the dynamic coupling between the local and global degrees of freedom, and f_q are the generalized external forces associated with the model's degrees of freedom.

In our case, given the nature of the problem, and the fact that we consider static deformations only, it makes sense to simplify the equations of motion by setting the mass density to zero, which will still preserve useful first-order dynamics that achieve equilibrium. Setting the mass density μ to zero causes the mass matrix M and the inertial forces g_q to vanish (Park et al., 1996a; Haber et al., 2000). This results in the first-order dynamic system (Park et al., 1996b)

$$D \frac{\partial q}{\partial t} + Kq = f_q. \quad (2)$$

Because these equations lack an inertial term, the system comes to rest as soon as all the forces equilibrate or vanish. We use D as a stabilizing factor only, and do not impose physical damping, which cannot be measured from experimental data. Therefore we assume that D is diagonal and constant over time, and set it equal to the identity matrix ($D = I$). Therefore the breast model is deformed using the following reduced form of Lagrange's equation of motion:

$$\alpha I \frac{\partial q}{\partial t} + Kq = f_q, \quad (3)$$

where the vector q contains the displacement degrees of freedom, α is a numerical damping constant and the vector f_q contains the total external forces due to body forces which in our case would be gravity. We are modeling the compression of the breast for a patient in a prone position. The breast is immobile in a state of equilibrium (the skin is mainly responsible for counteracting the effects of the gravitational force), and the plates compressing the breast move in a direction orthogonal to that of the gravitational forces. Therefore the vector f_q can be set to zero.

We may approximate the equation by using the finite element method described previously. Through this method, all quantities necessary for the Lagrange equations of motion are derived from the same quantities computed independently within each finite element. The various matrices and vectors involved in the Lagrange equations of motion are assembled from matrices computed within each of the elements.

Therefore in our algorithm we do not assemble the model stiffness matrix K , but work with the elemental stiffness matrices K_e , and assemble the forces around the nodes. Compared to the classical theory, this method is equivalent to a relaxation method, i.e. calculating the residuals at the nodes.

Stiffness (represented by the K matrix) can also be viewed as an internal resistance which results in a force

equal to $-\mathbf{K}\mathbf{q}$. Lagrange's equation of motion can then be written for each and every node i in the model as (Haber et al., 2000)

$$\alpha \mathbf{I} \frac{\partial \mathbf{q}_i}{\partial t} = \mathbf{f}_{i,\text{total}} = \mathbf{f}_{i,\text{internal}}, \quad (4)$$

where \mathbf{q}_i is the 3D nodal displacement at node i , $\mathbf{f}_{i,\text{internal}} = [-\mathbf{K}\mathbf{q}]_i$ is an internal stiffness force. The nodal equation becomes

$$\alpha \mathbf{I} \frac{\partial \mathbf{q}_i}{\partial t} = \mathbf{f}_{i,\text{internal}}, \quad (5)$$

where α is a numerical damping constant, which we set to 1. The time-discretized nodal equation can then be written as

$$\mathbf{q}_{i,t+1} = \mathbf{q}_{i,t} + \Delta t \cdot \mathbf{f}_{i,\text{internal}}. \quad (6)$$

At each displacement iteration, we integrate the equation using an Euler method with adaptive step sizing. The step size Δt is inversely proportional to the integration error. Since the forces multiply the time step, the adaptive step sizing effectively modulates the strength of the forces, thereby making the solution converge much faster than with a simple Euler integration technique (Haber et al., 2000). We compute two estimates of $\mathbf{q}_{i,t+1}$, $\mathbf{q}_{i,a}$ by taking an Euler step of size Δt , and $\mathbf{q}_{i,b}$ by taking two Euler steps of size $\Delta t/2$. Since $\mathbf{q}_{i,a}$ and $\mathbf{q}_{i,b}$ differ from each other by $O(\Delta t^2)$, a measure of the current error is $e = \sum_{i=1}^n |\mathbf{q}_{i,a} - \mathbf{q}_{i,b}|$, where the error is over the sum of the displacement errors of all nodes. If we are willing to have an error of as much as e_A , then the new step size can be written as $\Delta t_{\text{new}} = \sqrt{e_A/e} \cdot \Delta t$. The numerical integration ends when the difference between the sum of all displacements from one time iteration to the next is less than a predetermined threshold.

3.4. Internal forces due to stiffness

The degrees of freedom of the model are the 3D displacements of the finite element nodes. In our formulation, stiffness is represented as an internal nodal force $\mathbf{f}_{i,\text{internal}}$. The element force vector \mathbf{f}_e contains the forces on the element nodes: $\mathbf{f}_e = [\mathbf{f}_{i,\text{internal}}, \mathbf{f}_{i+1,\text{internal}}, \dots, \mathbf{f}_{i+n-1,\text{internal}}]^T$ where $\mathbf{f}_{i,\text{internal}}$ is the internal force on node i , and n is the number of nodes in the element. \mathbf{f}_e is calculated for each element as

$$\mathbf{f}_e = \mathbf{K}\mathbf{q}_e,$$

where \mathbf{q}_e contains the element's nodal displacements: $\mathbf{q}_e = [\mathbf{q}_i, \mathbf{q}_{i+1}, \dots, \mathbf{q}_{i+n-1}]^T$. The elemental stiffness matrix, \mathbf{K}_e , incorporates the geometry, material properties of the element and is a triple integral over the volume V_e of the element. It is computed from

$$\mathbf{K}_e = \iiint_{V_e} \mathbf{B}^T \mathbf{D} \mathbf{B} \, dV. \quad (8)$$

The matrix \mathbf{D} contains the material property information (which includes the value of the material's elastic modulus $E_k(\epsilon_k)$) and relates nodal stresses $\boldsymbol{\sigma}$, to nodal strains $\boldsymbol{\epsilon}$,

$$\boldsymbol{\sigma} = \mathbf{D}\boldsymbol{\epsilon}. \quad (9)$$

The matrix \mathbf{B} relates nodal strains to displacements, and incorporates Cauchy's infinitesimal strain tensor formulation (see Eq. (1)),

$$\boldsymbol{\epsilon} = \mathbf{B}\mathbf{q}_e. \quad (10)$$

Once the element forces are calculated, each element contributes to the total internal nodal force $\mathbf{f}_{i,\text{internal}}$ for each of its nodes. A detailed derivation of the finite element formulation for calculating the stiffness matrix, \mathbf{K} , is presented in (Zienkiewicz and Taylor, 1989).

3.5. Modeling large deformations

Compressing a breast using compression plates results in a large compression of the breast, meaning that the total compression distance between the two plates decreases by more than 10%. In order to model such large deformations, we divide the large deformation compression into a number of much smaller displacement steps. For every displacement step, we make use of small strain theory. Strain is calculated using Cauchy's infinitesimal strain tensor formula (given in the unabridged notation (Fung, 1994)),

$$\begin{aligned} \epsilon_{xx} &= \frac{\partial u}{\partial x}, & \epsilon_{yy} &= \frac{\partial v}{\partial y}, & \epsilon_{zz} &= \frac{\partial w}{\partial z}, \\ \epsilon_{xy,yx} &= \frac{1}{2} \left(\frac{\partial u}{\partial y} + \frac{\partial v}{\partial x} \right), & \epsilon_{xz,zx} &= \frac{1}{2} \left(\frac{\partial u}{\partial z} + \frac{\partial w}{\partial x} \right), & \epsilon_{yz,zy} &= \frac{1}{2} \left(\frac{\partial v}{\partial z} + \frac{\partial w}{\partial y} \right). \end{aligned} \quad (11)$$

$u = u(x, y, z)$, $v = v(x, y, z)$, $w = w(x, y, z)$ are the displacement fields in the x , y and z directions, respectively, from one small displacement iteration to another.

The main advantage of using small strain formulation lies in its simplicity, ease of implementation and fast computation. However, being an incremental formulation, it could lead to an accumulation of discretization errors and in consequence, to a lack of accuracy (Szekely et al., 1998). A way to solve this potential problem would be to use a total Lagrange formulation (as the one we use for estimating the non-linear material properties of tissue from one displacement iteration to the next), in which every state is related to the initial configuration. However that would complicate the formulation and slow down the computation of the solution. We show in the phantom study that the incremental errors introduced by small strain formulation can be neglected for the purpose of this model and overall study.

3.6. Modeling non-linear material properties

Most biological tissues display both a viscous (velocity

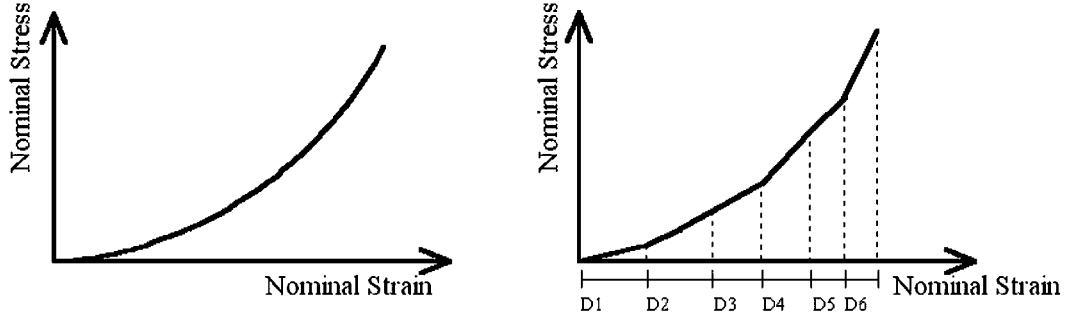


Fig. 3. Modeling a non-linear stress–strain curve (left) with a piecewise linear curve (right). D_i is the interval used during the i th deformation increment.

dependent) and elastic response; however, since we are only interested in slow displacements, the great majority of the forces developed can be attributed purely to the elastic response. All tissues involved in the breast can be considered:

- isotropic (Hayes et al., 1972; Krouskop et al., 1998),
- homogeneous (Sarvazyan et al., 1995; Skovoroda et al., 1995),
- incompressible (Fung, 1993),
- to have non-linear elastic properties (Fung, 1981; Zhang et al., 1997).

With these assumptions, it is possible to define the mechanical behavior of breast tissue using a single elastic modulus E_n , which is a function of strain ε_n for tissue type n (σ_n is the stress),

$$E_n = \frac{\partial \sigma_n}{\partial \varepsilon_n} = f(\varepsilon_n). \quad (12)$$

This non-linear relationship is calculated for every tissue type from uniaxial stress–strain experiments using tissue samples. The experimental curves are fit to a material model, which can be characterized using a small number of parameters. In order to model the non-linear mechanical behavior in every element, the following steps are followed, after every small deformation increment:

1. We calculate the Lagrangian strain tensor, \mathbf{E} , at the center of the element. \mathbf{E} is a measure of the deformation of a point in the model with respect to its initial position (a detailed description can be found in (Spencer, 1980)),

$$\mathbf{E} = \frac{1}{2}(\mathbf{F}^T \mathbf{F} - \mathbf{I}), \quad (13)$$

\mathbf{F} is the 3×3 -deformation gradient tensor, and its components can be written as

$$F_{pq} = \frac{\partial x_p}{\partial X_q}, \quad (14)$$

where x_p is one of the three components of \mathbf{x} , the final position vector, and X_q is one of the three components of \mathbf{X} the initial position vector. In our case, the final position of an element center point is after a given deformation increment, and the initial center point is

before the first deformation increment. \mathbf{I} is the identity matrix.

2. We calculate the maximum principal strain component, e_{\max} , which is given by the largest eigenvalue of the strain tensor \mathbf{E} .
3. Using the experimental stress–strain curve for the particular tissue type, the element is assigned a Young's modulus value corresponding to the slope of the curve at the strain measure e_{\max} : $E_n = f(e_{\max})$.

Therefore after every deformation increment, the element's stiffness value is updated to model the material's non-linear behavior. By doing so, we model a continuously differentiable stress–strain curve (in the limits of our deformations) as a continuous step-wise linear curve (Fig. 3).

4. Experimental design and methods

4.1. A phantom study

A deformable silicon gel phantom was built to study the movement of a stiff inclusion inside a deformable environment (as a tumor inside the breast) under plate compression (Azar et al., 2000). The phantom was imaged undeformed, then compressed. A 3D deformable model of the phantom was built from the resulting MR data, and was virtually compressed using custom-written software (*BreastView*). Another FEM of the phantom was built using a commercial pre-processor (PATRAN) from the phantom's directly measured dimensions, and was compressed virtually using a powerful commercial FEM software package (ABAQUS) which uses implicit integration schemes. The displacement vectors of the 8 corners of the stiff inclusion and its center were measured both from the MR images and from the two finite element models.

The explicit Finite Element formulation, which we implemented using small strain theory, may not always be as accurate as the implicit one, and time discretization errors can accumulate. The main reason is that our strain formulation is of an incremental form; this could lead to a lack of accuracy (Kojic and Bathe, 1987). The results of this phantom study show that the compressed model allows

us to track the position and motion of the stiff inclusion in the real compressed deformable environment. Furthermore, after comparing the compressed *BreastView* and ABAQUS models, the results also show that using a small strain approximation in our finite element formulation does not introduce a significant error.

Phantom construction. The phantom was designed to have magnetic properties (T1 and T2) similar to those of human breast tissue, to withstand large deformations (20% or greater), and to enable controlled deformations. The gel phantom was built using Sylgard Dielectric Gel 527 (Dow Corning, Midland, MI). A similar silicon gel (model Q7-2218, Dow Corning) has been suggested for use in MR imaging (Goldstein et al., 1987), and the same silicon gel was used to validate tagging with MR imaging to estimate material deformation (Young et al., 1993). The geometry of the deformable phantom consists of a rectangular box ($84 \times 82 \times 70$ mm) containing a rectangular inclusion ($20 \times 23 \times 20$ mm), which is 4.3 times stiffer than the surrounding silicon (Fig. 5). For more details about the silicon phantom construction, see Appendices A–C.

MR imaging of silicon phantom. The full silicon gel phantom was placed in a custom-built pressure device, where a pressure plate could compress the gel phantom in a similar way as with a real breast with the desired amount of deformation. The whole setup was secured firmly and imaged with a whole body 1.5-T superconducting magnet (GEMS, Milwaukee, WI). The silicon gel phantom was first imaged undeformed. The compression plate then applied a deformation width of 14% (9.8 mm) in the x -direction, and the phantom was imaged again. An axial and a coronal T1-weighted fast multi-planar gradient echo (FMPGR) sequences were performed in the uncompressed and compressed case.

Material properties of silicon phantom. The elastic properties of the phantom materials were evaluated on an Instron Model 1331 (Cambridge, MA) mechanical testing machine containing a semi-hydraulic computer driven system for very accurate tensile strength measurements. We used a load cell rated to 10 N. This load cell is certified to an accuracy of 0.01 N. Flat cylindrical samples of the silicone gel and the stiffer inclusion underwent uniaxial stress tests. Static load-deformation (stress–strain) curves were obtained.

The silicon gel can be assumed to be an isotropic hyperelastic material, and be described by a ‘strain energy potential’ which defines the strain energy stored in the material per unit of reference volume. The experimental data was fit to a law of rubberlike material known as the Mooney–Rivlin strain energy function (Green and Zerna, 1968; Spencer, 1980). The form of the Mooney–Rivlin strain energy potential is

$$U = C_{10}(\bar{I}_1 - 3) + C_{01}(\bar{I}_2 - 3) + \frac{1}{D_1}(J^{\text{el}} - 1)^2, \quad (15)$$

where U is the strain energy per unit of reference volume; C_{10} , C_{01} and D_1 are temperature-dependent material parameters; \bar{I}_1 and \bar{I}_2 are the first and second deviatoric strain invariants defined as $\bar{I}_1 = \bar{\lambda}_1^2 + \bar{\lambda}_2^2 + \bar{\lambda}_3^2$ and $\bar{I}_2 = \bar{\lambda}_1^{(-2)} + \bar{\lambda}_2^{(-2)} + \bar{\lambda}_3^{(-2)}$, where the deviatoric stretches $\bar{\lambda}_i = J^{-1/3} \lambda_i$; J is the total volume ratio; J^{el} is the elastic volume ratio, and λ_i are the principal stretches (defined as the ratios of current length to length in the original configuration in the principal directions of a material fiber). We assume that the silicon gel is incompressible and temperature independent (in the conditions of the experiment). Therefore, the strain energy potential expression can be simplified to

$$U = C_{10}(\bar{I}_1 - 3) + C_{01}(\bar{I}_2 - 3), \quad (16)$$

C_{10} and C_{01} are the material parameters to be determined experimentally.

The stress–strain relationship is developed using derivatives of the strain energy function with respect to the strain invariants. We define this relation in terms of the nominal stress T_U (the force divided by the original, undeformed area) and the nominal, or engineering strain ε_U (ratio of deformation length to length in the original configuration). The deformation gradient, expressed in the principal directions of stretch is

$$\mathbf{F} = \begin{bmatrix} \lambda_1 & 0 & 0 \\ 0 & \lambda_2 & 0 \\ 0 & 0 & \lambda_3 \end{bmatrix}, \quad (17)$$

where λ_1 , λ_2 and λ_3 are the principal stretches. Because we assume incompressibility and isothermal response, $J = \det(\mathbf{F}) = 1$ and, hence, $\lambda_1 \lambda_2 \lambda_3 = 1$. The deviatoric strain invariants in terms of the principal stretches are then $\bar{I}_1 = \lambda_1^2 + \lambda_2^2 + \lambda_3^2$ and $\bar{I}_2 = \lambda_1^{-2} + \lambda_2^{-2} + \lambda_3^{-2}$. The uniaxial deformation mode is characterized in terms of the principal stretches, λ_i as

$$\lambda_1 = \lambda_U, \quad \lambda_2 = \lambda_3 = 1/\sqrt{\lambda_U}, \quad (18)$$

where λ_U is the stretch in the loading direction. The strain energy potential expression can therefore be expressed solely in terms of λ_U ,

$$U = C_{10}(\lambda_U^2 + 2\lambda_U^{-1} - 3) + C_{01}(\lambda_U^{-2} + 2\lambda_U - 3). \quad (19)$$

To derive the uniaxial nominal stress T_U , we invoke the principle of virtual work ($\delta U = T_U \delta \lambda_U$) so that

$$T_U = \frac{\partial U}{\partial \lambda_U} = 2(1 - \lambda_U^{-3}) \cdot (\lambda_U C_{10} + C_{01}). \quad (20)$$

Now since the stretch λ_U is related to the nominal strain ε_U by $(\lambda_U = \varepsilon_U + 1)$, the nominal stress–strain relationship can finally be written as

$$T_U = 2[1 - (1 + \varepsilon_U)^{-3}] \cdot [(1 + \varepsilon_U)C_{10} + C_{01}]. \quad (21)$$

Eq. (21) was fit to the experimental stress–strain curves for the two types of silicon gel, using the least sum of squares method. The results are shown in Fig. 4. The average parameter values calculated are $C_{10} = 3740 \pm 64$ N/m², $C_{01} = 1970 \pm 34$ N/m² for the surrounding silicone gel, and $C_{10} = 16300 \pm 815$ N/m², $C_{01} = 10490 \pm 524$ N/m² for the silicone gel inclusion.

4.1.4. Phantom models

The first model was built using the *BreastView* software (see Fig. 5 bottom) (Azar et al., 2000). The other model of the phantom was built directly from its physical dimensions using a pre-processor program MSC/PATRAN (MSC, CA), which automatically meshed the model. Both FEMs consist of 21 slices (each 4 mm thick), stacked along the *z*-axis. The number of nodes in the *x*- and *y*-directions is 18 and 22, respectively, in order to have square-shaped volume elements. The finite element models are made of 7497 elements each. The element material properties were given a homogeneous, isotropic, Mooney-Rivlin hyperelastic model, with the C_{10} and C_{01} constants as measured above. The boundary conditions were applied appropriately, and the 9.8 mm displacement of the pressure plate was modeled in the initial conditions as a 9.8 mm displacement constraint on every node, which belongs to the displaced surface of the phantom.

The finite element modeling simulations were done using:

1. A robust finite element code ABAQUS (ABAQUS/Standard V.5.8, 1998), commercially available. Each element was modeled as a hybrid incompressible solid eight-node brick, which allows a fully incompressible constraint at each material calculation point (ABAQUS/Standard V.5.8, 1998).
2. The *BreastView* software in which 12 displacement iterations were used to compress the model. In each displacement iteration, a compression of 0.8167 mm was applied to the relevant boundary nodes in the model. This represents an average nominal strain of 1.16%, which can be considered small strain. The

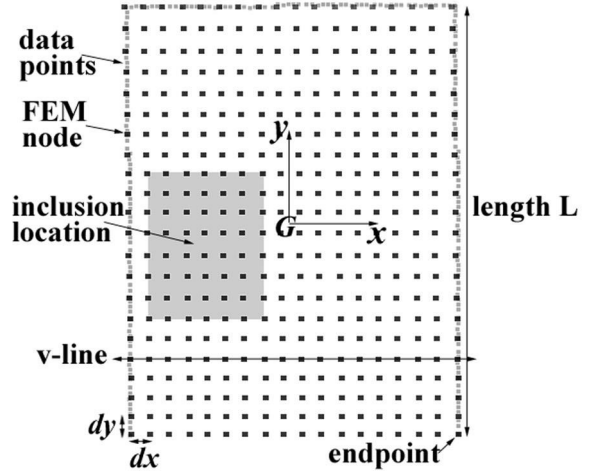
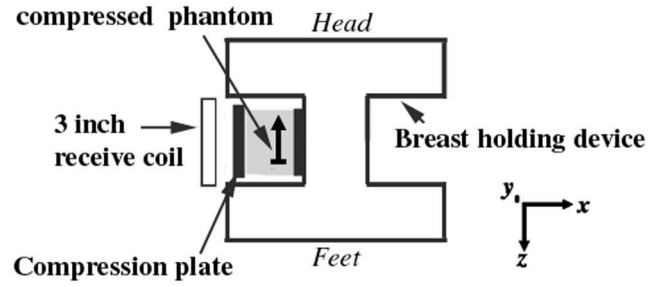


Fig. 5. Top view of the setup for imaging the compressed gel phantom (top), and construction of phantom model: 2D axial slice shown (bottom).

maximum allowed error of integration e_A in the adaptive algorithm, was chosen to be 1/1000th of the smallest dimension in the model d_{\min} , which is the smallest distance between two consecutive nodes: $d_{\min} = 3.90$ mm, and $e_A = 3.90 \times 10^{-3}$ mm. This ensured full convergence of the solution after each displacement iteration.

4.2. A patient study

A healthy patient's left breast was used to track the displacement of specific landmarks under plate compression. We found a small cyst inside the breast, which was

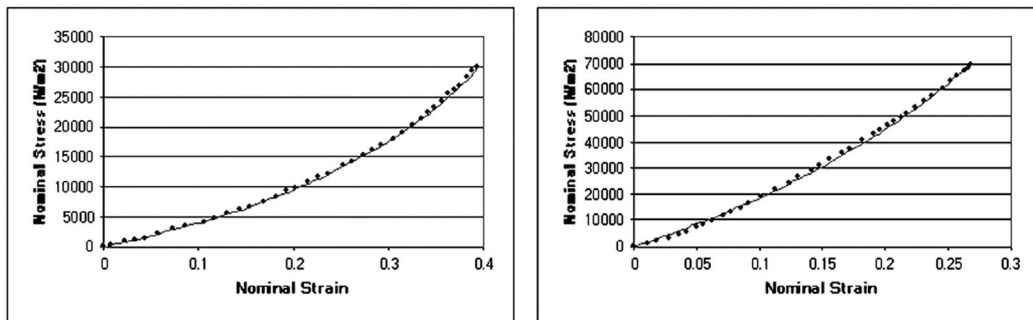


Fig. 4. Least-squares fit between the average experimental stress–strain curves (shown as dots), and the Mooney-Rivlin model (shown as a continuous line), for the surrounding silicone gel material (left), and the stiff inclusion gel material (right).

Table 1
Plate to plate distances before and after compression

	Plate to plate distance (mm)	Compression amount (mm)
Uncompressed	64.8 ± 0.9	0.0
Compressed	47.7 ± 0.9	17.1 ± 1.8

used as the inner landmark for tracking displacements inside the breast after compression. Additionally, two vitamin E pills were taped on the superior and inferior parts of the breast.

4.2.1. Patient breast MR data acquisition

The breast was imaged using a 1.5 Tesla machine Signa Horizon Echospeed (GEMS). 3D image sets were obtained under plate pressure conditions. The entire breast was imaged medially to laterally, from the visible rib cage to the nipple. The MR acquisition sequence was a 3D fast SPGR (T1 weighted), with a TR of 11.3 ms, a TE of 4.2 ms and a 25° flip angle. We used a phased array multi-coil. 124 slices each with a 0.9 mm thickness were acquired sagittally (left to right). Each slice had a field of view of 230×230 mm (256×256 pixels). This amounts to having cubic voxels with 0.9 mm sides.

4.2.2. Displacements due to plate compression

Usually, two compression plates are used to compress the breast (Table 1 shows the plate to plate distances). We make the following assumptions, which correspond to the actual breast compression setup (see Fig. 5(top), and Fig. 6):

- the plates are parallel to the y -axis;
- the plates move in the direction of the x -axis, towards

the breast, in a way that displacements can be considered static;

- the total compression distance D_{tot} for a plate is from its first point of contact with the breast to its final resting position.

Once the physical parameters are known, such as the plate length L_p , the distance from its tip to the patient's rib cage D_r , and the total compression distance D_{tot} , we translate those parameters into prescribed displacements to all individual model surface nodes which come in contact with the plate.

The total compression distance is translated into m_{tot} number of displacement iterations. A simple collision detection algorithm determines which node i comes in contact with the plate at each displacement iteration. Each of these nodes is assigned a prescribed displacement increment d_{ni} repeated in every iteration for which the plate is in contact with the node. Therefore the number of iterations for every surface node i varies and is denoted m_{ni} .

4.2.3. Boundary conditions

Let $X_i = (x_i, y_i, z_i)$ be the position of node i in the model (X_i is also a function of time t), $q_i = (q_{i,x}, q_{i,y}, q_{i,z})$ represent the displacement degrees of freedom for every node i in the model. The boundary conditions are applied to the displacement degrees of freedom as follows:

- *Base of the breast:* All nodes in the first two planes at the base of the breast model are fixed, and represent the patient rib cage area. This provides the support structure and fixes the breast model in space. Mathematically this is represented by

$$\forall \text{ nodes } i \in \{\text{base of the breast}\}, \begin{cases} q_{i,y} = 0, \\ q_{i,z} = 0. \end{cases}$$

- *Interface between breast and rib cage:* The nodes which are part of the breast tissue in contact with the rib cage, are allowed to slide against the nodes which represent the rib cage. Mathematically this is represented by: $\{y_i \geq y_{\text{Rib cage},i}(t=0)\}$.
- *Contact with the lateral plate:* boundary conditions between the virtual plate and the breast model could cause increased displacement errors for the nodes close to the edges of the virtual plate due to possible large rotational effects at the edges. However since we are concerned with lesion displacement, which is most generally located far enough from the plate edges, we can neglect errors due to rotations in the vicinity of the plate's edges. Additional experiments were done in order to determine whether the breast skin slides against the compression plates, or whether it sticks to them. Three different patient breasts were compressed and imaged using the same protocol as in interventional procedures. A vitamin E pill was attached to the skin of the patient breast directly in contact with the compression

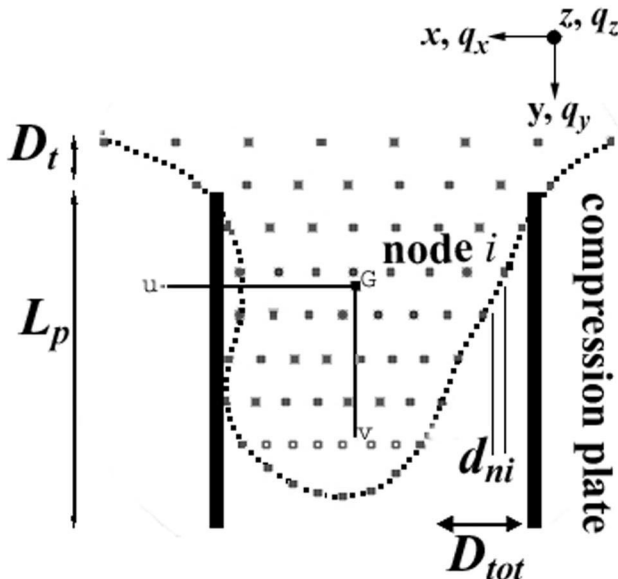


Fig. 6. Axial slice of model showing initial displacement parameters.

sion plate. The total average displacement for the three vitamin E pills (compressed–uncompressed) was 8.8 ± 1.3 mm ($x = 7.8 \pm 0.9$ mm; $y = 4.2 \pm 0.9$ mm). The results show that there is a sliding effect between the skin and the compression plate. We approximate the sliding by allowing the boundary nodes in the model directly in contact with the virtual compression plate, to slide against the plate. Mathematically this is represented by

\forall nodes $i \in \{\text{lateral side of breast}\}$,
 if (node i in contact with lateral plate)
 then $\{q_{i,x} = d_{ni}\}$,

where d_{ni} is the prescribed displacement at every contact iteration for node i .

- *Contact with the medial plate:* In principle, the patient breast is supposed to be pushed against the medial compression plate as much as possible, in order to increase contact with the plate, and decrease motion artifacts when using the lateral plate. In practice, the initial prone lying position of the patient determines how close the breast is to the medial plate; it is quite common that the breast is not completely pushed against the medial plate, and accounts for uncertainties in terms of the contact and boundary conditions between the breast and the medial plate.

In order to minimize the uncertainty and possible sources of error that may result, we model a real one-plate compression, with a virtual two-plate compression. We suppose that the left plate does all the compression and the right plate remains immobile. Then instead of applying the full compression amount using only the left virtual plate as would be expected, we divide that compression amount evenly, and both left and right virtual plates apply each half of the compression amount. However, after every compression step, the entire breast model is translated back a distance equal to half of the total compression amount, parallel and in the direction of the immobile right plate. In this way, it appears that the model is compressed using only one moving virtual plate. We will compare that method to the one-plate virtual compression, and choose the method, which yields the best results. Mathematically this is represented by

\forall nodes $i \in \{\text{medial side of breast}\}$,
 if (node i in contact with medial plate)
 then $\{q_{i,x} = d_{ni}\}$,

where d_{ni} is the prescribed displacement at every contact iteration for node i .

The breast was imaged first uncompressed, then imaged under plate compression. The breast compression device, made by GEMS, stabilized the patient's breast well enough to minimize motion artifacts between image sets. The compression plates were able to slide perfectly in the

sagittal direction and were locked in position when the desired compression was achieved. The displacements can therefore be considered static.

In order to help track the movement of the breast, we taped to the surface of the breast two vitamin E pills (one towards the superior part, the other one towards the inferior part) which appear as bright spots on the MR images: these serve as landmarks. The pills were taped to the breast in such a way that they do not come into contact with the compression plates, and did not influence the boundary conditions between the compression plates and the breast skin. Gadolinium pills were embedded inside the compression plates. These also appear as bright spots on the MR images, and allowed us to confirm the compression distance between the two plates. The right plate (on the breast's medial side) was kept immobile, while the left plate (on the lateral side) was moved to compress the breast.

4.2.4. Patient breast deformable model

A model of the patient breast was constructed from the given MR data, the boundary conditions, and the applied displacements, using *BreastView*. The different breast tissues inside the breast were modeled. The breast data was segmented semi-automatically, starting at the intersection of the outer side of one compression plate and the breast, all the way to the other plate.

The deformable model of the breast was built using every other slice out of the experimental data set, and discarding the outer slices, which did not contain useful information. A total of 58 slices was used. The breast model consists therefore of 58 slices (each slice in the uv -plane) stacked up along the z -axis. There are 8 nodes in the x -direction and 8 nodes in the y -direction in every slice. The full model contains 3712 nodes, 2793 3D hexahedral elements, 2394 2D triangular elements, and is shown in Fig. 7.

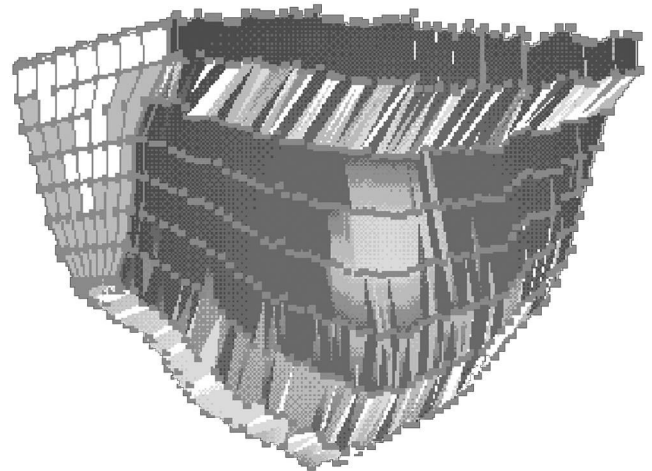


Fig. 7. Full breast model.

4.2.5. Mechanical measurements of human breast tissue and skin

Fig. 9(right) shows the major structures of a typical mature pre-menopausal breast. The dimensions and weight of the breast can greatly vary per individual. The breast is an inhomogeneous structure containing many layers of many different kinds of tissue. However the two predominant types of tissue within the breast are fat and normal glandular tissue, which supports lactation. The mammary gland forms a cone with its base at the chest wall and its apex at the nipple. Normal skin thickness lies between 0.5 and 1 mm. The superficial layer (fascia) is separated from the skin by 0.5–2.5 cm of subcutaneous fat. Tentacle-like prolongations of fibrous tissue extend in all directions from this fascia to the skin; these are called Cooper's ligaments. In the adult mammary gland, there are 15–20 irregular lobes, converging to the nipple through ducts 2–4.5 mm in diameter (Egan, 1988a). These ducts are immediately surrounded by dense connective tissue, which acts as a supporting framework. The glandular tissue is supported by estrogen; when a woman reaches menopause the estrogen levels decrease and the glandular tissue atrophies and eventually disappears, leaving only fat and skin (Harris et al., 1996).

Carcinomas in affected breasts are usually accompanied by local changes in material properties, due to increased stiffness in the lesion, as well as its shape and size (Egan, 1988b). There are several types of breast cancer; however, the most common are ductal carcinoma (which begins in the lining of the milk ducts of the breast), and lobular carcinoma (which begins in the lobules where breast milk is produced) (NCI, 1998).

Few studies have been made on determining the mechanical properties of tissue in the breast; however, average values of Young's modulus have been calculated for fat, glandular tissue, and cancer tissue (Skovoroda et al., 1995; Krouskop et al., 1998; Lawrence et al., 1999). Since we need non-linear stress–strain curves describing the mechanical behavior of breast tissue, we will use the mechanical properties of breast tissue determined by Wellman and Howe (1998). Exponential curves (which have been used in the past for several different tissue types (Fung, 1993)) are used to describe the stress–strain properties of breast tissue, following experimental stress–strain curves obtained from uniaxial loading of breast tissue. The fresh tissue samples were tested in the operating room within 10 minutes of excision, were kept hydrated by periodic application of saline solution, and were tested at room temperature ($21 \pm 2.5^\circ\text{C}$) (Wellman and Howe, 1998; Wellman, 1999). The exponential curves describing the elastic modulus E_n for tissue type n , are given by

$$E_n = \frac{\partial \sigma_n}{\partial \varepsilon_n} = b \cdot e^{m \varepsilon_n}, \quad (22)$$

where σ_n and ε_n are the nominal stress and strain,

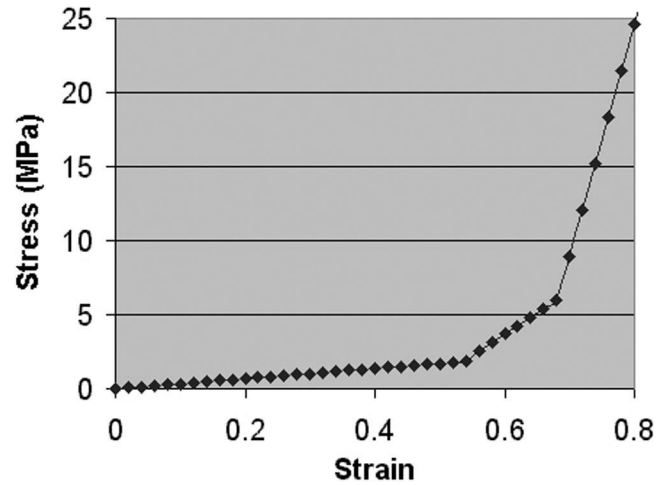


Fig. 8. Piecewise linear stress–strain curve for skin (Elden, 1977).

respectively, for tissue type n . b and m are the fit parameters determined experimentally for every tissue type:

- $b_{\text{glandular}} = 15\,100\text{ N/m}^2$,
- $m_{\text{glandular}} = 10.0$ (within 1 S.D.),
- $b_{\text{fat}} = 4460\text{ N/m}^2$,
- $m_{\text{fat}} = 7.4$ (within 1 S.D.),

We used a value of 0.49999 for Poisson's ratio.

The mechanical properties of skin have been studied more thoroughly than those of breast tissue, and several papers have been written on the subject (Veronda and Westmann, 1970; Agache et al., 1980; Fung, 1981; Schneider et al., 1984). Though it is not a homogeneous material, in many cases skin can be simplified to be statistically homogeneous (at higher strains it was found that the slope in the linear region of the stress–strain curve is similar in all directions) (Maurel et al., 1998). The typical experimental stress strain curve for skin (Elden, 1977) is transformed into a piecewise linear stress–strain curve which we will use to describe the mechanical properties of skin in the breast model (as shown in Fig. 8).

The stress–strain relationship for skin is of the form

$$\sigma_{\text{skin}} = a_i \cdot \varepsilon_{\text{skin}} + b_i, \quad (23)$$

where (a_i, b_i) are the parameters for every linear segment of the curve ($i=1-3$).

Then the elasticity modulus is given by

$$E_{\text{skin}} = a_i \quad (i=1-3). \quad (24)$$

The parameter values are shown in Table 2.

Table 2
Parameters for skin material model (N/m^2)

Parameter name	Line segment 1	Line segment 2	Line segment 3
a_i (N/m^2)	3.43×10^6	2.89×10^7	1.57×10^8
b_i (N/m^2)	0	-1.36×10^7	-1.01×10^8
Valid strain range	$0 \leq \varepsilon \leq 0.54$	$0.54 < \varepsilon \leq 0.68$	$0.68 < \varepsilon \leq 1$

4.2.6. Modifications of fat tissue model

The rationale underlying the modification of the fatty tissue model is based on the fact that ex vivo measurements of fatty tissue properties, although accurate, always ignore the supporting structure of fibers in the breast. Also those measurements are almost always made at room temperature, which significantly affects the mechanical properties of fatty tissue, since fatty tissue is almost liquid at body temperature (Krouskop et al., 1998) (on average 10–15°C higher than room temperature).

None of the experimental measurements of breast tissue encountered in the literature take into account the supporting structure of fibers including Cooper's ligaments to describe the mechanical behavior of fatty tissue in vivo. We also know from the literature, and from testing with other tissue types, how the absolute value of the tissue modulus may be affected by the boundary conditions (confinement) acting on a sample. Confinement can be significantly different from organ to organ depending on its surrounding environment (Krouskop et al., 1998).

We hypothesize that:

- the supporting structure of fibers, including Cooper's ligaments, compartmentalizes fatty tissue, and prevents it from being squeezed out of its location;
- as fatty tissue is being compressed, the local pressure increases and leads to an increase in the apparent stiffness value of fat.

These hypotheses are supported by the experimental evidence of the numerous compressed patient breast images scanned to date using MRI. These data show fatty tissue clearly not squeezed out but actually remaining in its location as the breast is being compressed, as shown in Fig. 9.

We test the hypotheses by updating the material model, such that the stiffness of fatty tissue is made to increase up to an average stiffness value of glandular tissue: as fatty tissue is being compressed and compartmentalized, the local pressure in the compartment increases and leads to an increase in the apparent stiffness value of fat, until the stiffness reaches that of the glandular tissue. Given this hypothesis, we can set the following necessary boundary conditions for E_{fat} :

$$\begin{aligned}
 &\text{If } \varepsilon_{\text{fat}} = 0 : E_{\text{fat}}(0) = b_{\text{fat}} \\
 &\text{If } \varepsilon_{\text{fat}} \leq \varepsilon_{\text{limit}} : b_{\text{fat}} \leq E_{\text{fat}} \leq E_{\text{gland}} \\
 &\quad \frac{\partial E_{\text{fat}}}{\partial \varepsilon_{\text{fat}}} \geq 0 \\
 &\text{If } \varepsilon_{\text{fat}} = \varepsilon_{\text{limit}} : E_{\text{fat}} = E_{\text{gland}} = b_{\text{gland}} e^{m_{\text{gland}} \varepsilon_{\text{limit}}} \equiv \alpha \\
 &\quad \frac{\partial E_{\text{fat}}}{\partial \varepsilon_{\text{fat}}} = \frac{\partial E_{\text{gland}}}{\partial \varepsilon_{\text{gland}}} = b_{\text{gland}} m_{\text{gland}} e^{m_{\text{gland}} \varepsilon_{\text{limit}}} \equiv \beta \\
 &\text{If } \varepsilon_{\text{fat}} \geq \varepsilon_{\text{limit}} : E_{\text{fat}} = E_{\text{gland}}
 \end{aligned} \tag{25}$$

These boundary conditions merely state the fact that E_{fat} is a continuous smooth non-decreasing function.

The simplest equation, which satisfies the above conditions, is a quadratic equation of the form

$$E_{\text{fat}}(\varepsilon_{\text{fat}}) = A \cdot \varepsilon_{\text{fat}}^2 + B \cdot \varepsilon_{\text{fat}} + C. \tag{26}$$

Solving for A , B and C given the boundary conditions, yields the following:

$$\begin{aligned}
 A &= \frac{\beta \cdot \varepsilon_{\text{limit}} + b_{\text{fat}} - \varepsilon}{\varepsilon_{\text{limit}}^2}, \\
 B &= \frac{2\alpha - 2b_{\text{fat}} - \beta \cdot \varepsilon_{\text{limit}}}{\varepsilon_{\text{limit}}}, \\
 C &= b_{\text{fat}}.
 \end{aligned} \tag{27}$$

There is a condition on $\varepsilon_{\text{limit}}$ which comes from the necessity that $(E_{\text{fat}})' \geq 0$; this is equivalent to writing $(E_{\text{fat}})'(0) \geq 0$ as long as $A > 0$. This leads to the condition that $\varepsilon_{\text{limit}} \leq 2 \cdot (\alpha - b_{\text{fat}}) / \beta$. The curve describing $E_{\text{fat}}(\varepsilon_{\text{fat}})$ is shown in Fig. 10 using the experimentally derived values for b_{gland} , m_{gland} and b_{fat} . We solved for the maximum allowed strain limit, and used it to model fatty tissue. We find $\varepsilon_{\text{limit}} = 15.5\%$.

We test the updated fatty tissue model hypothesis, and the value of $\varepsilon_{\text{limit}}$, in the sensitivity analysis, where the effect of varying the material parameters on the model performance is investigated. Rather than modeling the structure and geometry of Cooper's ligaments, we model their functionality and overall effect.

5. Results and discussion

5.1. Silicon phantom experiment

The axial slice going through the center of the inclusion is shown in Fig. 11(top) in the uncompressed and in the compressed mode. As expected the edges of the phantom have changed shape as well as the edges of the tumor. Because silicon is incompressible, the side deformations of the phantom are quite large.

Because it is important in the real case to track the displacement of a cancer tumor in the breast, we tracked the displacement of the inclusion in the phantom. By using image analysis software, we measured the displacement vectors of the center of the inclusion, as well as its eight corners. We used the axial slices to measure the x and y displacements, and the coronal slices to measure the z displacements (the positions of the various points of interest were calculated from the MR images with respect to the position of the non-moving bottom edge of the silicon phantom).

5.1.1. ABAQUS simulation results

Fig. 11(bottom) shows the displacement vectors of the inclusion corners and center from MR Data (bottom left), and from the ABAQUS model (bottom right). The average

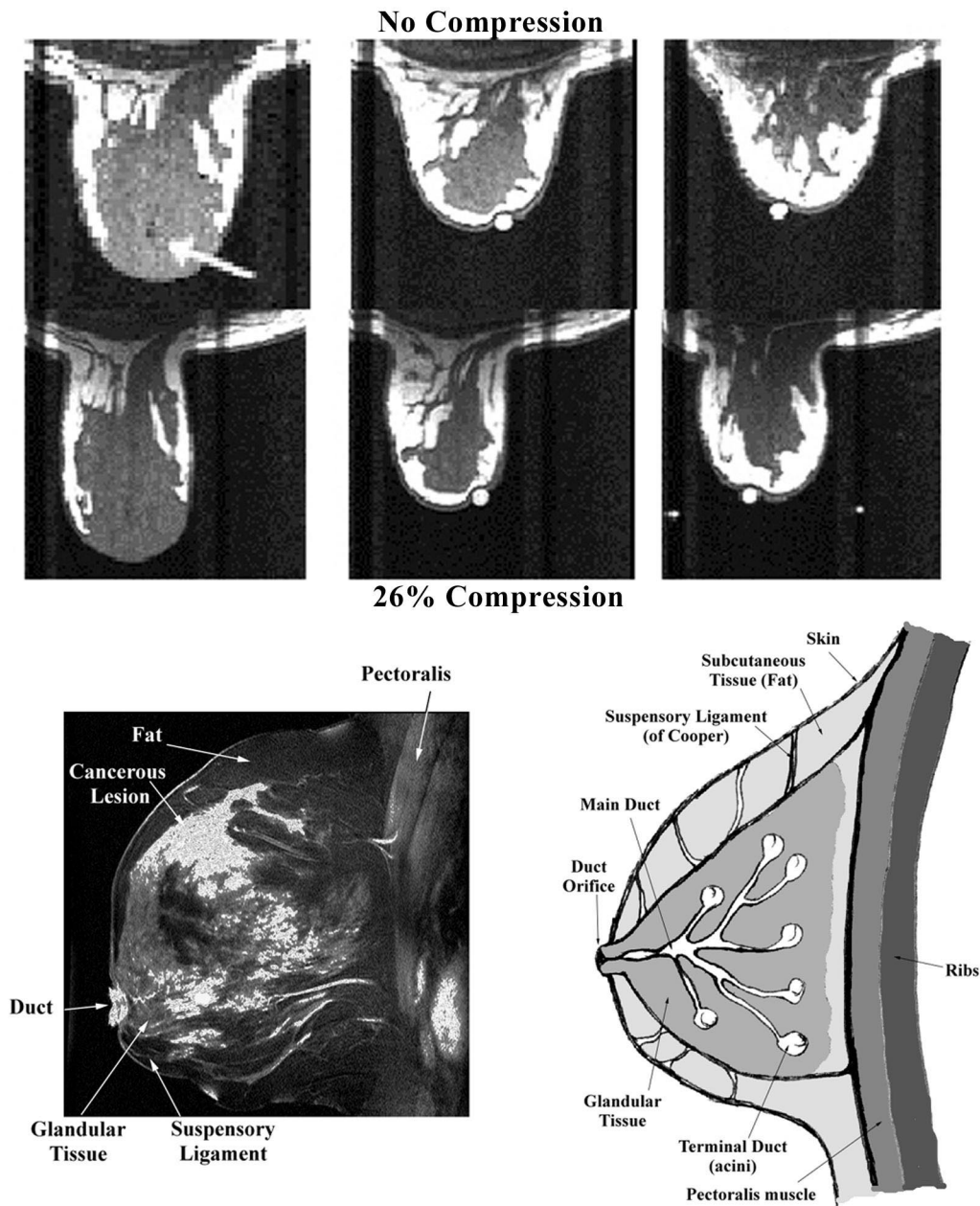


Fig. 9. Example of fatty tissue compartmentalization (left), and structure and location of Cooper's ligaments (right).

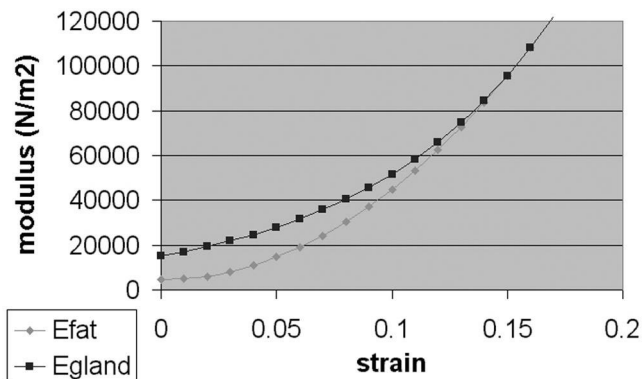


Fig. 10. Fat material properties curve.

errors in displacements were 0.34, 0.66 and 0.40 mm in the x , y and z directions, respectively, and are within the maximum imaging error.

5.1.2. BreastView simulation results

Fig. 12(left) shows a comparison between the *BreastView* and ABAQUS simulated virtual compressions. The displacement errors between the BreastView, ABAQUS simulations and the MR results are shown in Fig. 12(right). The results show that the displacement errors between the two simulations and the MR data are very close and within

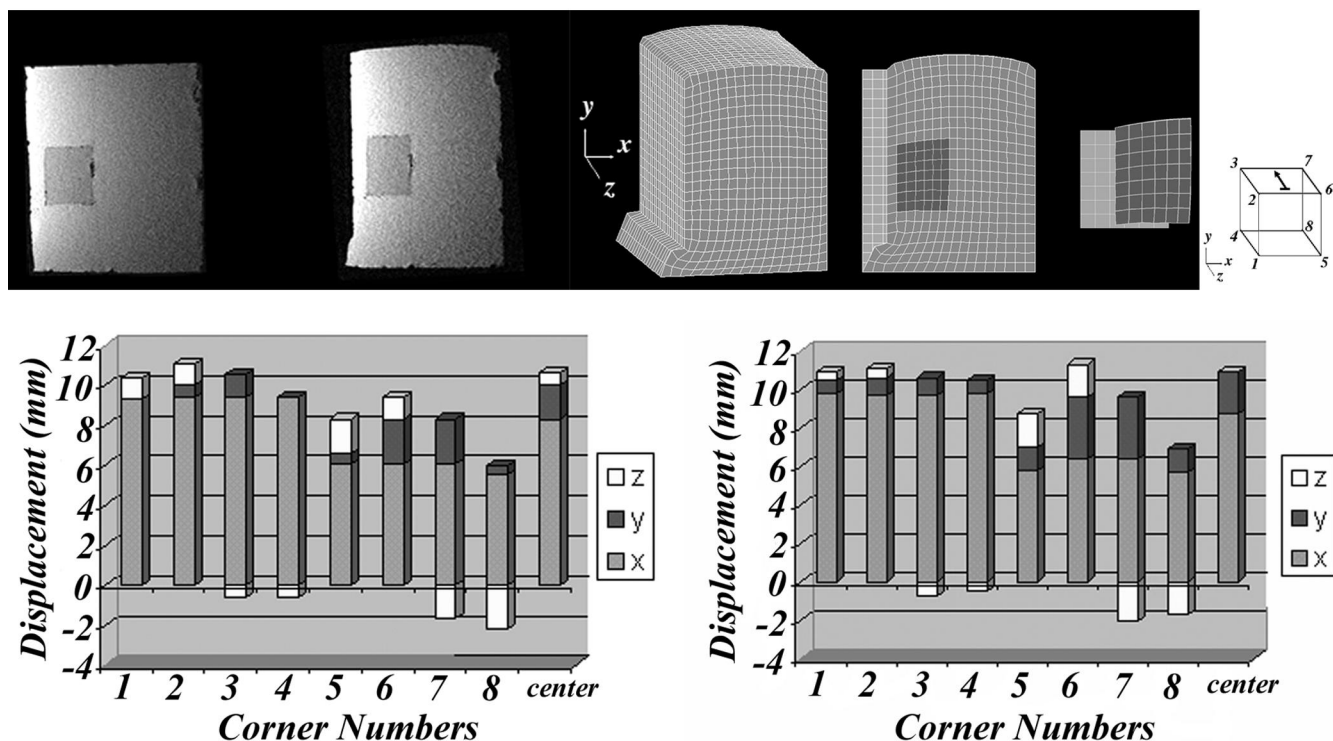


Fig. 11. Uncompressed and compressed axial MR slice of phantom (top left), 3D view of model including axial slice through center of inclusion and axial view of inclusion center, before and after compression (top right), displacement vectors of inclusion corners and center from MR data (bottom left), and from the ABAQUS model (bottom right).

the imaging error magnitude. Furthermore, all of the average displacement errors per node between the two simulations are under 1 mm.

This silicon phantom study shows that

- the compressed model allows us to track the position and motion of the stiff inclusion in the real compressed deformable environment;
- after comparing the compressed *BreastView* and ABAQUS model results, using a small strain approximation instead of the Lagrangian finite strain expression, in our finite element algorithm does not introduce a significant error in simulations of large deformation.

5.2. Patient breast compression experiment

5.2.1. MR results

Table 3 shows the displacement vectors of the cyst inside the breast, and the two vitamin E pills after compression. The displacement measurements (in mm) were made using Scion Image software. In order to compute the cyst and vitamin E pills displacements, we calculated the positions of the breast cyst and vitamin E pills with respect to the position of the gadolinium pills embedded in the non-moving compression plate. The edge points of the vitamin E pills closest to the skin were used

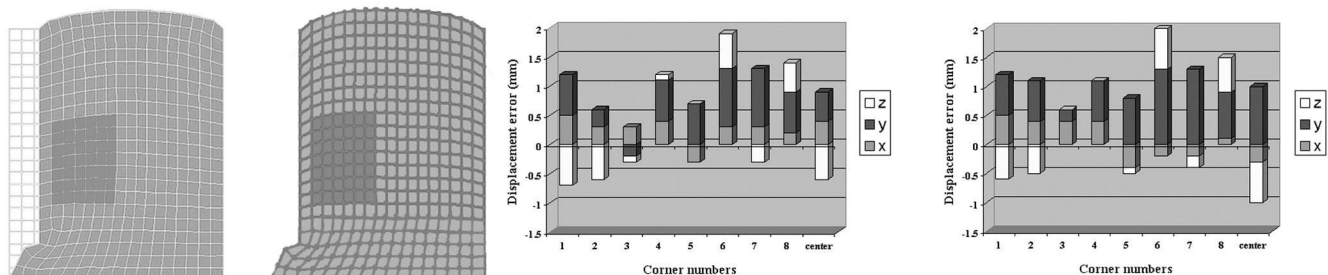


Fig. 12. Axial slice going through the inclusion after compression, in the ABAQUS simulation (left model), and in the *BreastView* simulation (right model); displacement errors of inclusion corners and center: ABAQUS-MR (left diagram), *BreastView*-MR (right diagram).

Table 3

Displacement vectors (mm) of the landmarks obtained experimentally (compressed–uncompressed)

	Vitamin E pill (superior)			Vitamin E pill (inferior)			Small cyst		
	x	y	z	x	y	z	x	y	z
Compression	−9.0	3.6	2.7	−7.2	0.9	−3.6	−6.3	1.8	1.8

in the calculations. The images in Fig. 13 show the axial cross-sections of the patient's left breast.

5.2.2. Variational study

The effect of varying different parameters is investigated. Several parameters describing the model are varied over a physiologically relevant range, and every time the model simulation is done, the displacement of the landmarks, as well as other relevant performance assessment parameters are recorded.

First, we decide which of the one-plate or two-plate virtual compression yields the best results. Then after a convergence analysis we decide whether the slab model (variable z -mesh density) can replace the full model in the virtual compression; this would dramatically decrease the simulation time. Finally we do a material properties sensitivity analysis to show how sensitive is the model performance to variations in material parameters.

5.2.3. Performance assessment parameters

Two performance assessment parameters are used in the variational study:

- *Displacement difference* ($\text{DISP}_{\text{diff}}$): Difference (Model–Real) of displacement, of inclusion center of gravity, where inclusion can be lesion, cyst, or vitamin E pill.

$$\text{DISP}_{\text{diff}} = (\sqrt{X_{\text{diff}}^2 + T_{\text{diff}}^2 + Z_{\text{diff}}^2}). \quad (28)$$

- *% Misclassification* (%MIS): Compares the number of

misclassified pixels in the model with the compressed MRI.

$$\% \text{MIS} = \text{NMIS} / \text{TNUM}, \quad (29)$$

where NMIS is the number of misclassified pixels in model with respect to compressed MR dataset ((nonfat pixels in fat elements) + (nonglandular pixels in glandular elements) + (nontumor pixels in tumor elements)), and TNUM is the total number of breast pixels in the MR dataset.

The displacement differences are used to assess the performance of the most important result in the model, which is how well the displacement of an inclusion in the real breast, can be predicted using the model. The misclassification percentage is a value, which gives an idea of how well the model globally predicts the displacement of the major structures in the breast.

Therefore the displacement difference offers a local measure of performance, whereas the misclassification percentage offers a global ‘macroscopic’ measure of the performance of the breast model.

5.2.4. Initial uncompressed model and uncompressed MR images

The uncompressed MR images containing the landmarks and the corresponding uncompressed model slices are shown in Fig. 14. The arrows in the figure indicate the location of the landmarks.

All of the simulations in the variational studies were done on a SGI Octane Workstation with two 195 MHz IP30 processors (MIPS R10000 processors), and 256 megabytes of memory (RAM). The first step in the variational analysis is to decide what type of model to use, and what type of virtual compression to apply. Given the different parameters outlined above, the virtual compression was done using one then two virtual compression plates, with the full model and the slab model. The displacement differences and percent misclassifications are shown in Fig. 15.

5.2.5. One-plate versus two-plate virtual compressions for the full model

The full model consists of 58 slices stacked up along the axial axis. Each slice contains 8×8 nodes, for a total of 3712 nodes, 2793 3D hexahedral elements, and 2394 2D triangular elements. This experiment is aimed at compar-

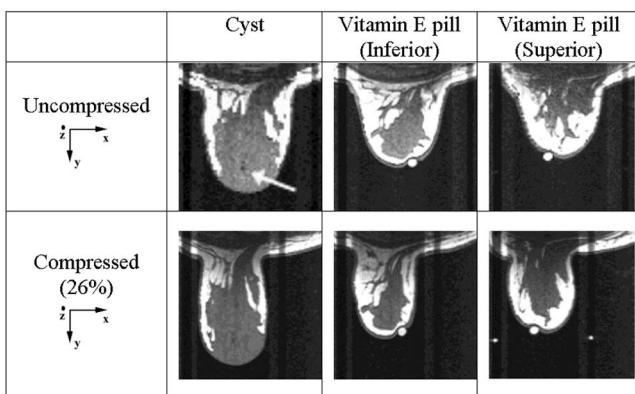


Fig. 13. MR Slices containing the landmarks, for the uncompressed and compressed cases.

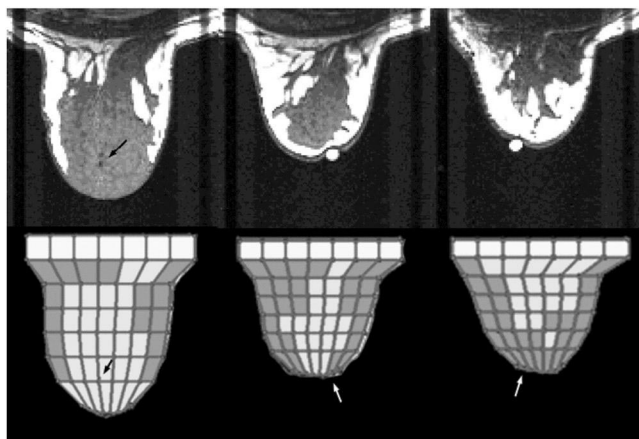


Fig. 14. Uncompressed MR images (top), and uncompressed model slices (bottom).

ing the performance of the virtual one-plate compression simulation to that of the virtual two-plate compression simulation, where the total compression amount is evenly divided between the two virtual compression plates.

Clearly from the results shown above, the two-plate virtual compression yielded better results than the one-plate virtual compression, using the full model.

The percent misclassifications for the slices containing the vitamin E pills are high compared to that of the slice containing the cyst. This higher level of inaccuracy is due to the fact that the former slices belong to the outer edges of the patient's breast; the contact and boundary conditions between these slices and the compression plates is not always clear, and it is very difficult to accurately predict their deformation for that reason.

5.2.6. Convergence analysis

We did a convergence analysis in the (x,y) direction: the (x,y) mesh density was increased, and the model compression was done. We recorded the total displacement of the cyst. Another convergence analysis was done in the z -direction, using the slab model: the z -direction mesh density was varied using the slab-model algorithm, increasing the number of model slices around the point of interest. We recorded the total displacement of the cyst. The number of displacement iterations was increased (as the displacement per iteration was decreased in order to keep the same total virtual plate compression of 17 mm). The analysis was done on the displacement of the cyst in the model. All the results are shown in Fig. 16.

The analysis shows that the simulation indeed converges to the solution, as the model mesh is refined. Also using about 10 displacement iterations per simulation step proves enough for convergence of the solution. Furthermore, using the slab model with only 8 slices instead of 56 does not decrease the performance of the simulation. In order to show the performance of the slab model, we ran the entire simulation using that model. The slab model contains 512 nodes, 343 3D hexahedral elements, and 294 2D triangular elements. As shown in Fig. 17, the mesh density in the slab model is the highest around the points of interest (cyst, Fig. 17(center) or vitamin E pill, Fig. 17(right)). The results from the simulation are shown below.

When comparing the results in Fig. 18(top) to Fig. 15 we see that the performance of the slab model was as good as that of the full model. This enables us to run the simulation dramatically faster since the slab model contains many less elements than the full model.

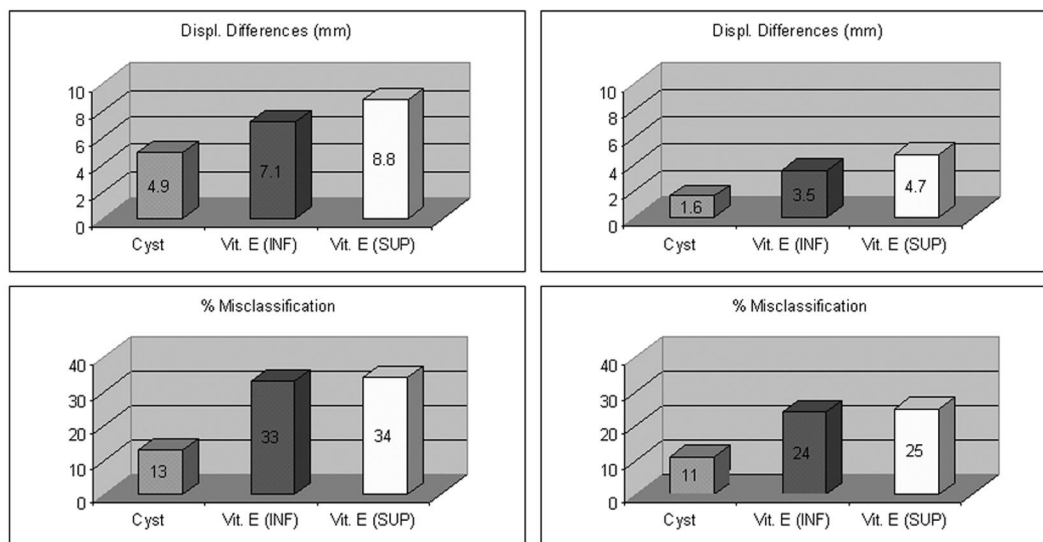


Fig. 15. Displacement differences (mm) and percent misclassifications in the one-plate virtual compression (left), and in the two-plate virtual compression (right), with the full model.

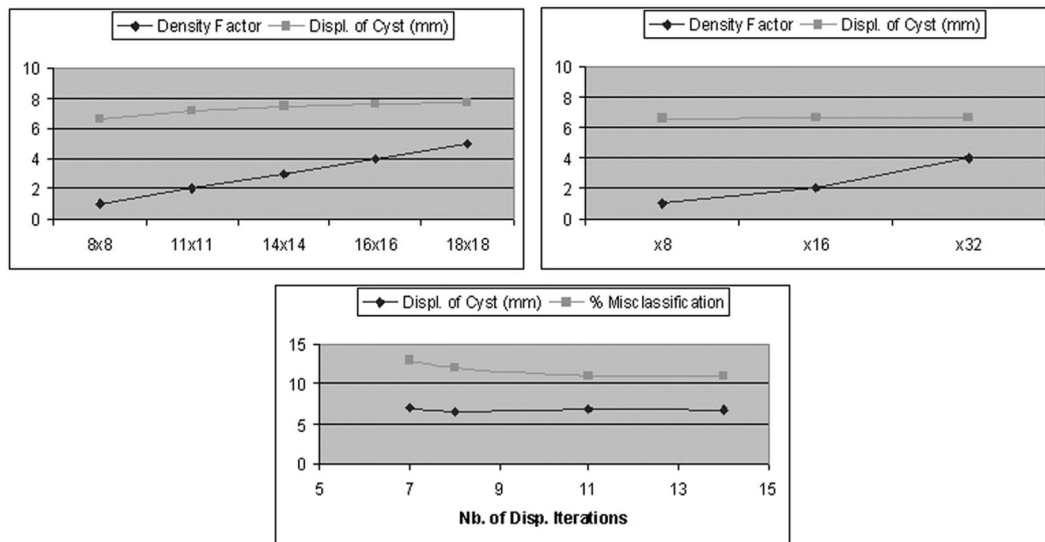


Fig. 16. Convergence analysis in the (x,y) direction (top left), convergence analysis in the z-direction (top right), and convergence analysis with the number of displacement iterations per simulation step (bottom). The density factor on the top two graphs represents the total number of nodes in the model, normalized by the number of nodes in the model with 8×8 nodes in the (x,y) direction.

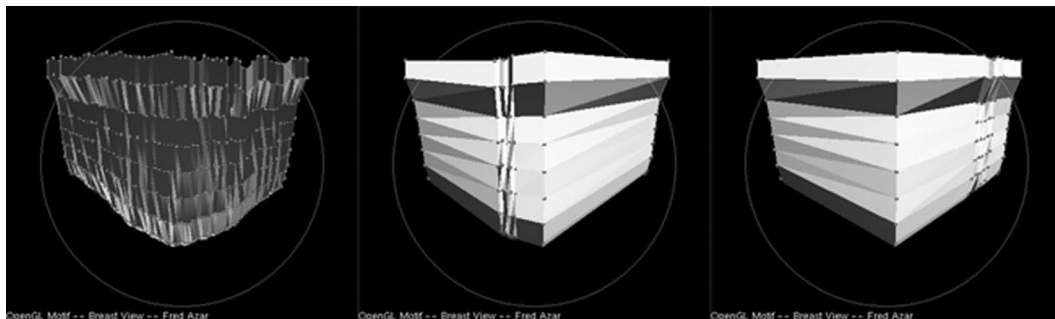


Fig. 17. Full breast model mesh (left), and variable meshes around different points of interest (cyst, center and vitamin E pill, right).

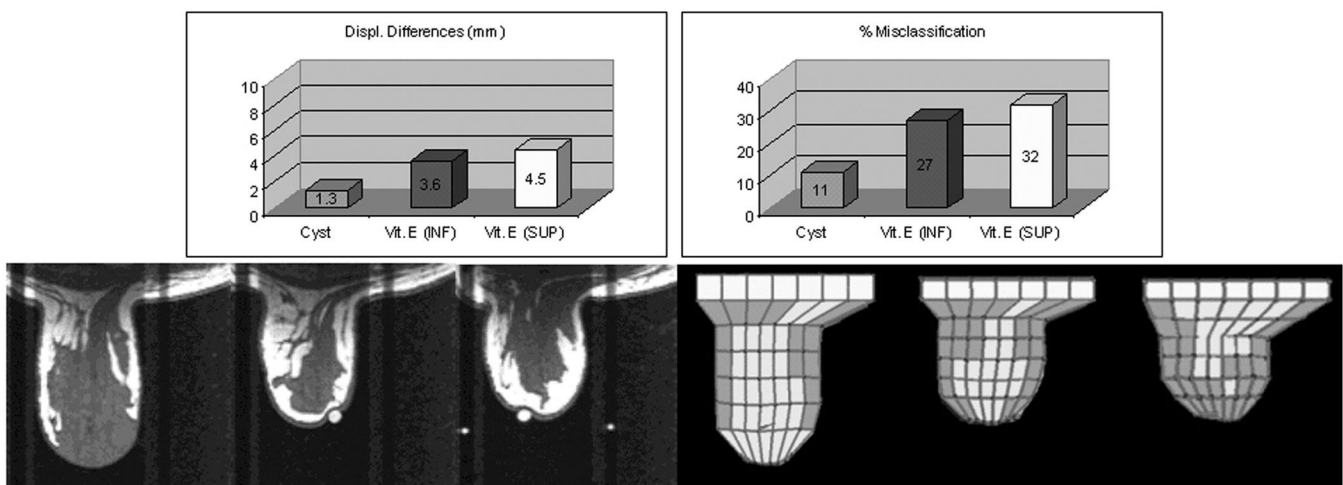


Fig. 18. Displacement differences (mm, top left), and percent misclassification (top right) in the two-plate virtual compression with the slab model; compressed MR slices (bottom left), and corresponding virtually compressed model slices (bottom right) after a two-plate virtual compression using the slab model.

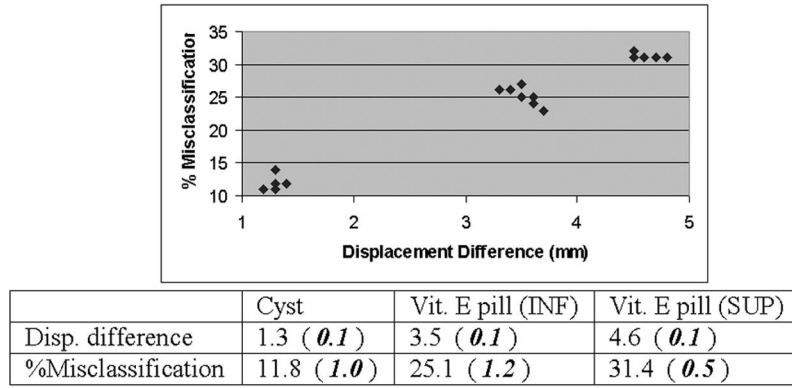


Fig. 19. Graph showing sensitivity analysis results (top), and table showing averages and standard deviations (in parentheses) of sensitivity analysis (bottom). Each point in the sensitivity analysis represents a modeling experiment with one of the material parameters varied. We can clearly distinguish three different clusters. The lower left cluster represents results from the cyst displacement, the middle cluster represents results from the vitamin E pill (inferior) displacements, and the upper right cluster represents results from the vitamin E pill (superior) displacements.

5.2.7. Material properties sensitivity analysis

The effects of varying the different material properties parameters are investigated. The parameters are varied over a physiologically relevant range, within 2 S.D. of their average experimentally derived value. The numerical values of the relevant material properties used in our chosen model were varied within ± 1.2 S.D., one at a time. The parameter for the new updated fat model was varied by 30%, then by 60%. The material parameters of interest which were varied are m_{gland} , b_{gland} for the glandular material model, and e_{limit} for the new updated fat model. All of the results are shown in Fig. 19, where the displacement differences versus percent misclassifications are graphed. Each point represents a modeling experiment with one of the material parameters varied. We can clearly distinguish three different clusters. The lower left cluster represents results from the cyst displacement, the middle cluster represents results from the vitamin E pill (inferior) displacements, and the upper right cluster represents results from the vitamin E pill (superior) displacements.

6. Additional comments

6.1. Potential sources of error

Three types of discretization errors can occur, first errors from the finite element method, then errors from the time domain discretization (solving the dynamic equations), and finally errors from the non-linear material properties model.

6.1.1. Sources of error from the finite element method

Errors in the finite element method can be divided into two classes:

- discretization errors resulting from geometric differences between the boundaries of the model and its finite element approximation;

- modeling errors, due to the difference between the true solution and its shape function representation.

Using smaller elements can reduce discretization errors — the errors tend to zero, as the element size tends to zero. Shape function errors do not decrease as the element size reduces and may thus prevent convergence to the exact solution or even cause divergence.

An important property of isoparametric elements is that they provide C^0 continuity, and contain a complete linear polynomial in Cartesian coordinates (Ergatoudis et al., 1968). Therefore isoparametric elements satisfy the two criteria required of the shape functions to guarantee convergence.

6.1.2. Sources of error from the time domain discretization

The time-discretized nodal equation is

$$\mathbf{q}_{i,t+1} = \mathbf{q}_{i,t} + \Delta t \mathbf{f}_{i,\text{internal}} \quad (30)$$

At every displacement iteration, we integrate Eq. (30) using the adaptive Euler technique (Press et al., 1992; DeVries, 1994), where the time step Δt , varies according to the amount of integration error.

We can make the integration error sufficiently small to insure convergence of the solution. The numerical integration ends when the difference between the sum of all displacements from one time iteration to the next is less than a threshold ($10^{-3}\%$ is shown to be a good assumption),

$$\text{difference} = \sum_{i=1}^n |\mathbf{q}_{i,t+1}| - \sum_{i=1}^n |\mathbf{q}_{i,t}| < \text{threshold} \quad (31)$$

Fig. 20 show that a difference between two consecutive displacements, of less than $10^{-3}\%$ is enough to claim convergence of the model.

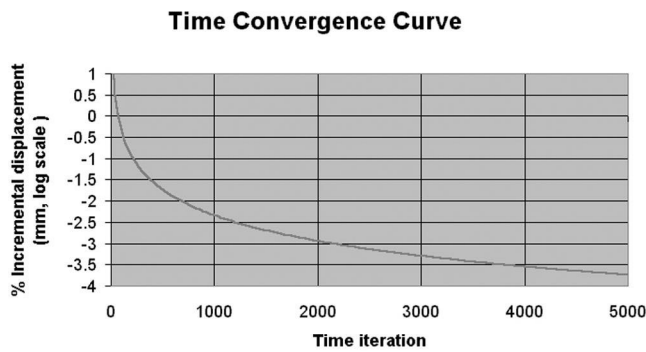


Fig. 20. Time convergence curve: percent incremental displacement (log scale).

6.1.3. Sources of error from material properties measurements

It is difficult to assert the absolute significance of the material models developed (Fung, 1972). Furthermore, the actual complexity of breast tissue (anisotropy, inhomogeneity, the number and distribution of Cooper's ligaments) prohibits us from accurately calculating a 3D map of a patient's breast tissue properties. This is why only average values of experimentally derived material models are used in our finite element analysis. The non-linear stress–strain curve describing the mechanical behavior of breast tissue, is discretized into a number of different segments, each corresponding to a displacement iteration. In order to test the effect of material properties model discretization, the number of displacement iterations was increased (as the displacement per iteration was decreased in order to keep the same total virtual plate compression). The analysis was done on the displacement of the cyst in the model.

As shown in the convergence analysis with the number of displacement iterations per simulation step (Fig. 16), increasing the number of displacement iterations, which also means increasing the number of linear segments discretizing the non-linear material stress–strain curve, leads to a convergence of the two important result parameters in the model. However the variation in the parameters do not exceed 15% for the percent misclassification, and 14% in the displacement of the cyst. Once again since only average values of experimentally derived material models are used in the analysis, the accuracy involved in the stress–strain curve discretization is not as important as the accuracy involved in approximating the shape of the breast in the model.

The material properties sensitivity analysis (Fig. 19) shows that large variations in material properties parameters (± 1.2 S.D.) do not significantly affect the parameter results. This may be explained by the fact that the breast is under pressure: since glandular and fatty tissue make up the majority of breast tissue, and since the fat material model eventually becomes equivalent to the glandular tissue material model at a certain level of strain, then

material properties difference may become of secondary importance in the simulations. If that is the case, then we may be able to simplify the material properties models and thus increase the speed of the breast compression simulation.

6.2. Specific properties of reliability

The model performance is as reliable as the parameter that is most sensitive to variations in the conditions of the experiment. In our model, it is shown, that the physical representation of the breast is most sensitive in variations of the breast shape. It is also shown through the material properties sensitivity analysis, that the performance of the model has modest dependence to variations in material properties within 1–2 S.D.

Indeed, the shape and size of a patient breast influence the amount of compression on the breast, and the boundary properties between the breast and the compression plates. For example, when testing the performance of the two-plate virtual compression in the slab model, the displacement differences (in mm) were 1.3, 3.6 and 4.5 for the cyst, inferior vitamin E pill, and superior vitamin E pill, respectively. The percent misclassifications were 11, 27 and 32%. It is clear that the cyst's displacement was predicted more accurately than the displacement of the vitamin E pills. This difference in accuracy is due to the fact that the vitamin E pills were placed on the outer edges of the patient's breast, where the contact and boundary conditions between the breast and the compression plates are not always clearly defined, and it may become difficult to accurately predict breast deformation at these locations.

Therefore additional experiments would be needed in order to assess the reliability of the model by choosing a number of patients with breasts of different sizes, leading to different initial and boundary conditions for the model.

6.3. Major novelties in the model

The major novelties in this model include:

- The updated fatty tissue material model, which takes into account the effect of fat compartmentalization due to Cooper's ligaments in the breast: we showed through empirical evidence that fat compartmentalization occurs as the breast is being compressed, and that the new updated fatty tissue material model takes that phenomenon into account, and performs better than the original fatty tissue model.
- The use of small displacement iterations while updating the tissues' different material properties, in order to model the non-linear behavior of tissue material models: the silicon phantom study allowed us to compare predicted displacement of a silicon inclusion from an ABAQUS (large commercially available FEM package) simulation, and from a *BreastView* (our soft-

ware package) simulation, and showed that our algorithm does yield accurate results.

- The application of finite element modeling theory to model the deformation of a human female breast in such a way that the entire process takes less than a half-hour, which according to the clinicians consulted, is a reasonably short time duration.

7. Conclusion

Currently, high field (1.5 T) superconducting MR imaging does not allow live guidance during needle breast procedures. The current procedure allows the physician only to calculate approximately the location and extent of a cancerous tumor in the compressed patient breast before inserting the needle. It can then become relatively uncertain that the tissue specimen removed during the biopsy actually belongs to the lesion of interest. A new method for guiding clinical breast biopsy was presented, based on a deformable finite element model of the breast. The geometry of the model is constructed from MR data, and its mechanical properties are modeled using a non-linear material model. This method allows imaging the breast without or with mild compression before the procedure, then compressing the breast and using the finite element model to predict the tumor's position during the procedure.

The final results show that it is possible to create a deformable model of the breast based on the use of finite elements with non-linear material properties capable of modeling and predicting the deformation of the breast. This study also shows that the full procedure can be carried out in less than a half-hour: from start to end, the average times to completion were 12 minutes for segmentation of MR data, 3 minutes for the model mesh creation, and 14 minutes for the model simulation.

This deformable model may be used as a new tool to the physician (Azar et al., 2001), who will:

1. image the breast under little or no compression (thus increasing the contrast and visibility of the tumor),
2. build the deformable model of the breast from the data,
3. compress the breast as much as the patient will allow (to minimize deformations caused by the insertion of the needle),
4. virtually compress the breast model in the virtual environment using the same boundary conditions as in reality,
5. finally use the virtually compressed model to predict position of the real lesion within the real compressed breast during the procedure.

Future development in this project will be to develop a framework for a full-scale real-time Finite Element simulation of breast tissue deformation in more complex systems involving surgical instruments interacting with the model. The keys for such a development will include scalable

parallel solution algorithms (Szekely et al., 1998), as well as dedicated parallel hardware. The new system will allow real-time virtual surgical procedures of the breast, allowing the physician or student to fully prepare or train for the real procedure. The real-time capability will then allow the user to connect haptic devices such as a glove with pressure feedback, or a simulated needle with force feedback, and will bring the user one step closer to reality.

Acknowledgements

The authors are thankful to Norm Butler, Allen Bonner, Idith Haber, Reid Miller, Bruno Carvalho and Joe Giammarco for their help in various aspects of this work.

Appendix A. Modeling 8-node hexahedral solid isoparametric elements

Finite element shape functions. The shape functions are used to interpolate a motion variable (displacement, position) from the nodes to a point in the element. The shape functions for an eight-node brick element (or linear solid element) are

$$N_i = (1/8) (1 \pm \xi) (1 \pm \eta) (1 \pm \zeta), \quad (\text{A.1})$$

in which $i = 1, 2, \dots, 8$.

Finite element stiffness matrix. The derivation of the 3D finite element stiffness matrix presented follows the formulation found in (Cook et al., 1989). The finite element stiffness matrix K_e is given by

$$K_e = \iiint_{V_e} \mathbf{B}^T \mathbf{D} \mathbf{B} dV, \quad (\text{A.2})$$

where \mathbf{D} is the stress–strain matrix and \mathbf{B} is the strain–displacement matrix. The stiffness matrix incorporates the material and geometrical stiffness of the element.

Stress–strain matrix. Stress is related to strain through the following relationship, for a linear material,

$$\boldsymbol{\sigma} = \mathbf{D} \boldsymbol{\varepsilon}, \quad (\text{A.3})$$

where

$$\boldsymbol{\varepsilon} = \begin{bmatrix} \varepsilon_{xx} \\ \varepsilon_{yy} \\ \varepsilon_{zz} \\ \varepsilon_{xy} \\ \varepsilon_{zy} \\ \varepsilon_{xz} \end{bmatrix} \quad (\text{A.4})$$

and $\boldsymbol{\sigma}$ is a column vector with the respective strain components. For an isotropic material, \mathbf{D} is defined by

$$D = \frac{Y(1-\nu)}{(1+\nu)(1-2\nu)} \begin{bmatrix} 1 & \frac{\nu}{1-\nu} & \frac{\nu}{1-\nu} & 0 & 0 & 0 \\ & 1 & \frac{\nu}{1-\nu} & 0 & 0 & 0 \\ & & 1 & 0 & 0 & 0 \\ & & & \frac{1-2\nu}{2(1-\nu)} & 0 & 0 \\ & & & & \frac{1-2\nu}{2(1-\nu)} & 0 \\ & & & & & \frac{1-2\nu}{2(1-\nu)} \end{bmatrix}, \quad \text{Symmetric} \quad (\text{A.5})$$

where Y is the Young's modulus, and ν is the Poisson ratio.

Strain–displacement matrix. The matrix B relates strains to displacements at the nodes:

$$\boldsymbol{\varepsilon} = \mathbf{B} \mathbf{q}_e, \quad (\text{A.6})$$

where $\boldsymbol{\varepsilon}$ is given above, and \mathbf{q}_e is the displacements at the element's n nodes. For Cartesian coordinates, u , v , and w are displacements in the x , y and z directions, respectively:

$$\mathbf{q}_e = \begin{bmatrix} u_1 \\ v_1 \\ w_1 \\ u_2 \\ v_2 \\ w_2 \\ \vdots \\ u_n \\ v_n \\ w_n \end{bmatrix}. \quad (\text{A.7})$$

The relation between strain and displacements at the nodes involve matrix multiplications as defined below: First, the definition of small strain can be written in matrix form as

$$\boldsymbol{\varepsilon} = \underbrace{\begin{bmatrix} 1 & 0 & 0 & 0 & 0 & 0 & 0 & 0 & 0 \\ 0 & 0 & 0 & 0 & 1 & 0 & 0 & 0 & 0 \\ 0 & 0 & 0 & 0 & 0 & 0 & 0 & 0 & 1 \\ 0 & \frac{1}{2} & 0 & \frac{1}{2} & 0 & 0 & 0 & 0 & 0 \\ 0 & 0 & 0 & 0 & 0 & \frac{1}{2} & 0 & \frac{1}{2} & 0 \\ 0 & 0 & \frac{1}{2} & 0 & 0 & 0 & \frac{1}{2} & 0 & 0 \end{bmatrix}}_{L:6 \times 9} \begin{bmatrix} u_x \\ u_y \\ u_z \\ v_x \\ v_y \\ v_z \\ w_x \\ w_y \\ w_z \end{bmatrix}. \quad (\text{A.8})$$

The derivatives of displacement with respect to global coordinates in this equation can be related to derivatives of displacements with respect to local coordinates by the 9×9 matrix M , in the following equation:

$$\begin{bmatrix} u_x \\ u_y \\ u_z \\ v_x \\ v_y \\ v_z \\ w_x \\ w_y \\ w_z \end{bmatrix} = \underbrace{\begin{bmatrix} \Gamma_{11} & \Gamma_{12} & \Gamma_{13} & 0 & 0 & 0 & 0 & 0 & 0 \\ \Gamma_{21} & \Gamma_{22} & \Gamma_{23} & 0 & 0 & 0 & 0 & 0 & 0 \\ \Gamma_{31} & \Gamma_{32} & \Gamma_{33} & 0 & 0 & 0 & 0 & 0 & 0 \\ 0 & 0 & 0 & \Gamma_{11} & \Gamma_{12} & \Gamma_{13} & 0 & 0 & 0 \\ 0 & 0 & 0 & \Gamma_{21} & \Gamma_{22} & \Gamma_{23} & 0 & 0 & 0 \\ 0 & 0 & 0 & \Gamma_{31} & \Gamma_{32} & \Gamma_{33} & 0 & 0 & 0 \\ 0 & 0 & 0 & 0 & 0 & 0 & \Gamma_{11} & \Gamma_{12} & \Gamma_{13} \\ 0 & 0 & 0 & 0 & 0 & 0 & \Gamma_{21} & \Gamma_{22} & \Gamma_{23} \\ 0 & 0 & 0 & 0 & 0 & 0 & \Gamma_{31} & \Gamma_{32} & \Gamma_{33} \end{bmatrix}}_{M:9 \times 9} \begin{bmatrix} u_{,\xi} \\ u_{,\eta} \\ u_{,\zeta} \\ v_{,\xi} \\ v_{,\eta} \\ v_{,\zeta} \\ w_{,\xi} \\ w_{,\eta} \\ w_{,\zeta} \end{bmatrix}. \quad (\text{A.9})$$

The matrix M is composed of a 3×3 matrix, Γ , defined later. The derivatives of displacements with respect to local coordinates can now be related to the nodal displacements (vector \mathbf{q}_e) via the shape functions. We know that the interpolation functions define the displacement in the element in terms of nodal displacements. For example, the displacement in the x -direction, u , is

$$u = \sum_{i=1}^n N_i u_i = N_1 u_1 + N_2 u_2 + \dots + N_n u_n \quad (\text{A.10})$$

and the derivative with respect to a local coordinate, ξ , is

$$\begin{aligned} \frac{\partial u}{\partial \xi} &= u_{,\xi} = \sum_{i=1}^n N_{i,\xi} u_i \\ &= N_{1,\xi} u_1 + N_{2,\xi} u_2 + \dots + N_{n,\xi} u_n. \end{aligned} \quad (\text{A.11})$$

This relation follows for all 3 displacement derivatives taken with respect to the three local coordinates. It is written in matrix form as

$$\begin{bmatrix} u_{,\xi} \\ u_{,\eta} \\ u_{,\zeta} \\ v_{,\xi} \\ v_{,\eta} \\ v_{,\zeta} \\ w_{,\xi} \\ w_{,\eta} \\ w_{,\zeta} \end{bmatrix} = \underbrace{\begin{bmatrix} N_{1,\xi} & 0 & 0 & N_{2,\xi} & 0 & 0 & : & N_{n,\xi} & 0 & 0 \\ N_{1,\eta} & 0 & 0 & N_{2,\eta} & 0 & 0 & : & N_{n,\eta} & 0 & 0 \\ N_{1,\zeta} & 0 & 0 & N_{2,\zeta} & 0 & 0 & : & N_{n,\zeta} & 0 & 0 \\ 0 & N_{1,\xi} & 0 & 0 & N_{2,\xi} & 0 & : & 0 & N_{n,\xi} & 0 \\ 0 & N_{1,\eta} & 0 & 0 & N_{2,\eta} & 0 & : & 0 & N_{n,\eta} & 0 \\ 0 & N_{1,\zeta} & 0 & 0 & N_{2,\zeta} & 0 & : & 0 & N_{n,\zeta} & 0 \\ 0 & 0 & N_{1,\xi} & 0 & 0 & N_{2,\xi} & : & 0 & 0 & N_{n,\xi} \\ 0 & 0 & N_{1,\eta} & 0 & 0 & N_{2,\eta} & : & 0 & 0 & N_{n,\eta} \\ 0 & 0 & N_{1,\zeta} & 0 & 0 & N_{2,\zeta} & : & 0 & 0 & N_{n,\zeta} \end{bmatrix}}_{Q:9 \times (n \times 3)} \mathbf{q}_e. \quad (\text{A.12})$$

Thus, there are three matrix multiplications and the matrix B is composed of three matrices. Comparing the equations, we get

$$\underbrace{B}_{6 \times (n \times 3)} = \underbrace{L}_{6 \times 9} \underbrace{M}_{9 \times 9} \underbrace{Q}_{9 \times (n \times 3)}. \quad (\text{A.13})$$

Derivation of inverse Jacobian. The Jacobian relates derivatives in the global coordinate system (x, y, z) to derivatives in the local coordinate system (ξ, η, ζ) and can be simply derived using the chain-rule. So for a function $\Psi(x, y, z)$,

$$\begin{bmatrix} \Psi_{,\xi} \\ \Psi_{,\eta} \\ \Psi_{,\zeta} \end{bmatrix} = \underbrace{\begin{bmatrix} x_{,\xi} & y_{,\xi} & z_{,\xi} \\ x_{,\eta} & y_{,\eta} & z_{,\eta} \\ x_{,\zeta} & y_{,\zeta} & z_{,\zeta} \end{bmatrix}}_{J:3 \times 3} \begin{bmatrix} \Psi_{,x} \\ \Psi_{,y} \\ \Psi_{,z} \end{bmatrix}. \quad (\text{A.14})$$

In the isoparametric formulation, a point (x,y,z) in the element is interpolated from the nodes with the shape functions,

$$x = \sum_{i=1}^n N_i x_i, \quad y = \sum_{i=1}^n N_i y_i, \quad z = \sum_{i=1}^n N_i z_i, \quad (\text{A.15})$$

where the shape functions are functions of the local coordinates. Therefore, the elements in the Jacobian matrix can be evaluated by taking the derivative of the appropriate term in the last equation with respect to the appropriate local coordinates,

$$J = \begin{bmatrix} \sum_{i=1}^n N_{i,\xi} x_i & \sum_{i=1}^n N_{i,\xi} y_i & \sum_{i=1}^n N_{i,\xi} z_i \\ \sum_{i=1}^n N_{i,\eta} x_i & \sum_{i=1}^n N_{i,\eta} y_i & \sum_{i=1}^n N_{i,\eta} z_i \\ \sum_{i=1}^n N_{i,\zeta} x_i & \sum_{i=1}^n N_{i,\zeta} y_i & \sum_{i=1}^n N_{i,\zeta} z_i \end{bmatrix}. \quad (\text{A.16})$$

This formula for J can be expanded as follows:

$$J = \underbrace{\begin{bmatrix} N_{1,\xi} & N_{2,\xi} & N_{3,\xi} & N_{4,\xi} & \dots & N_{n,\xi} \\ N_{1,\eta} & N_{2,\eta} & N_{3,\eta} & N_{4,\eta} & \dots & N_{n,\eta} \\ N_{1,\zeta} & N_{2,\zeta} & N_{3,\zeta} & N_{4,\zeta} & \dots & N_{n,\zeta} \end{bmatrix}}_{D_n:3 \times n} \underbrace{\begin{bmatrix} x_1 & y_1 & z_1 \\ x_2 & y_2 & z_2 \\ x_3 & y_3 & z_3 \\ x_4 & y_4 & z_4 \\ \vdots & \vdots & \vdots \\ x_n & y_n & z_n \end{bmatrix}}_{x:n \times 3}. \quad (\text{A.17})$$

The matrix x contains the deformed positions of the n nodes in the element. The matrix F is finally given by

$$F = J^{-1} = \begin{bmatrix} F_{11} & F_{12} & F_{13} \\ F_{21} & F_{22} & F_{23} \\ F_{31} & F_{32} & F_{33} \end{bmatrix}. \quad (\text{A.18})$$

Appendix B. Modeling linear triangle isoparametric elements

Fig. 21 shows a triangular element $P_1P_2P_3$ in a local orthonormal coordinate system (α, β) with basis unit vectors $\hat{\alpha}$, $\hat{\beta}$ and its origin at node P_1 . The local node displacement vectors are given by (p_i, q_i) for every node i . The real-world 3D-coordinate system is given by (x,y,z) and the real-world 3D node displacements are given by (u,v,w) . The displacement field is given by $p = p(\alpha, \beta)$, and $q = q(\alpha, \beta)$. They are each interpolated from the *nodal displacement* degrees of freedom p_i and q_j ,

$$\begin{bmatrix} p \\ q \end{bmatrix} = N q_e, \quad \text{where } N = \begin{bmatrix} \xi_1 & 0 & \xi_2 & 0 & \xi_3 & 0 \\ 0 & \xi_1 & 0 & \xi_2 & 0 & \xi_3 \end{bmatrix}, \quad (\text{B.1})$$

$$q_e = \begin{bmatrix} p_1 \\ q_1 \\ p_2 \\ q_2 \\ p_3 \\ q_3 \end{bmatrix}.$$

ξ_i are the local area coordinates of any point P inside the triangle element: P divides the triangle element into three sub-areas A_1 , A_2 and A_3 . Area coordinates are defined as ratios of areas,

$$\xi_1 = \frac{A_1}{A}, \quad \xi_2 = \frac{A_2}{A}, \quad \xi_3 = \frac{A_3}{A}, \quad (\text{B.2})$$

where A is the area of the triangle element. Now since $A = A_1 + A_2 + A_3$, the ξ_i are not independent, and they satisfy the constraint equation

$$\xi_1 + \xi_2 + \xi_3 = 1. \quad (\text{B.3})$$

This constraint equation and the linear relation between

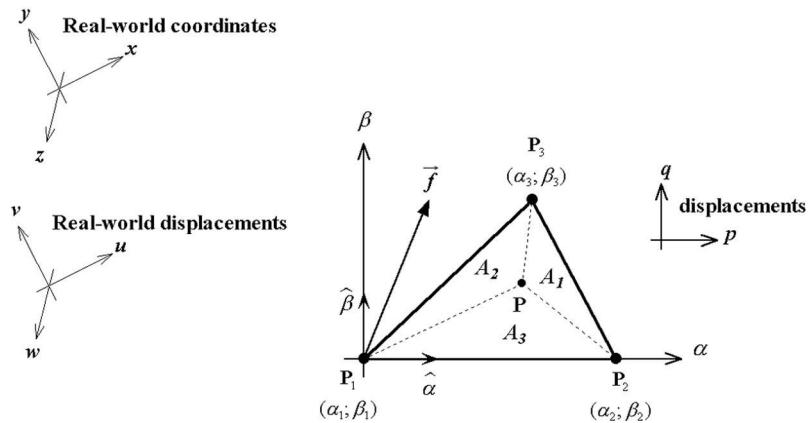


Fig. 21. Linear three-node triangle element.

Cartesian (α, β) and area (ξ_1, ξ_2, ξ_3) coordinates are expressed by the following equations:

$$\begin{bmatrix} 1 \\ \alpha \\ \beta \end{bmatrix} = A \begin{bmatrix} \xi_1 \\ \xi_2 \\ \xi_3 \end{bmatrix}, \quad (B.4)$$

$$\begin{bmatrix} \xi_1 \\ \xi_2 \\ \xi_3 \end{bmatrix} = A^{-1} \begin{bmatrix} 1 \\ \alpha \\ \beta \end{bmatrix},$$

where

$$A = \begin{bmatrix} 1 & 1 & 1 \\ \alpha_1 & \alpha_2 & \alpha_3 \\ \beta_1 & \beta_2 & \beta_3 \end{bmatrix}, \quad (B.5)$$

$$A^{-1} = \frac{1}{2A} \begin{bmatrix} (\alpha_2\beta_3 - \alpha_3\beta_2) & \beta_{23} & \alpha_{32} \\ (\alpha_3\beta_1 - \alpha_1\beta_3) & \beta_{31} & \alpha_{13} \\ (\alpha_1\beta_2 - \alpha_2\beta_1) & \beta_{12} & \alpha_{21} \end{bmatrix},$$

with $\alpha_{ij} \equiv \alpha_i - \alpha_j$ and $\beta_{ij} \equiv \beta_i - \beta_j$, and $2A = \det(A) = \alpha_{21}\beta_{31} - \alpha_{31}\beta_{21}$.

Since we know that strains are defined as $\varepsilon = B q_e$, and using the chain rule, we obtain the following expression for matrix B , after simplification:

$$B = \partial N = \frac{1}{2A} \begin{bmatrix} \beta_{23} & 0 & \beta_{31} & 0 & \beta_{12} & 0 \\ 0 & \alpha_{32} & 0 & \alpha_{13} & 0 & \alpha_{21} \\ \alpha_{32} & \beta_{23} & \alpha_{13} & \beta_{31} & \alpha_{12} & \beta_{12} \end{bmatrix}. \quad (B.6)$$

Material properties matrix D . D is defined as

$$D = \frac{Y}{(1+\nu)(1-2\nu)} \begin{bmatrix} (1-\nu) & \nu & 0 \\ \nu & (1-\nu) & 0 \\ 0 & 0 & \frac{(1-2\nu)}{2} \end{bmatrix}, \quad (B.7)$$

where Y =Young's modulus of elasticity; ν =Poisson ratio.

Element stiffness matrix formulation. Finally, the element stiffness matrix K_e is given by

$$K_e = \iiint_{V_e} B^T D B dV. \quad (B.8)$$

But B and D are constant over the triangle element, and we suppose that the element thickness t (which corresponds to the skin's thickness) is also constant. Then K_e can be simply written as

$$\underbrace{K_e}_{6 \times 6} = A t \cdot \underbrace{B^T}_{6 \times 3} \underbrace{D}_{3 \times 3} \underbrace{B}_{3 \times 6} \quad (B.9)$$

where A is the area of the triangle element.

Forces on element nodes. The forces generated on the element nodes P_1 , P_2 and P_3 are then written as

$$F_e = K_e q_e \Leftrightarrow \begin{bmatrix} \alpha_{F1} \\ \beta_{F1} \\ \alpha_{F2} \\ \beta_{F2} \\ \alpha_{F3} \\ \beta_{F3} \end{bmatrix} = K_e \begin{bmatrix} p_1 \\ q_1 \\ p_2 \\ q_2 \\ p_3 \\ q_3 \end{bmatrix}. \quad (B.10)$$

Expression for K_e in the real world coordinates. The node forces generated $(\alpha_{Fi}, \beta_{Fi})$, the node displacement vectors (p_i, q_i) and the node coordinates (α_i, β_i) need to be transformed from and to the real-world 3D coordinate system (x, y, z) . The basis vectors $\hat{\alpha}(x_{\hat{\alpha}}, y_{\hat{\alpha}}, z_{\hat{\alpha}})$ and $\hat{\beta}(x_{\hat{\beta}}, y_{\hat{\beta}}, z_{\hat{\beta}})$ in the (x, y, z) system are given by the following:

$$\hat{\alpha} = \frac{\vec{\alpha}}{\|\vec{\alpha}\|}, \quad \text{where } \vec{\alpha} = \overrightarrow{P_1 P_2},$$

$$\hat{\beta} = \frac{\vec{\beta}}{\|\vec{\beta}\|}, \quad \text{where } \vec{\beta} = \overrightarrow{P_1 P_3} - \frac{(\overrightarrow{P_1 P_2}) \cdot (\overrightarrow{P_1 P_3})}{\|\overrightarrow{P_1 P_2}\|^2} \overrightarrow{P_1 P_2}. \quad (B.11)$$

Coordinates of element nodes. The coordinates of the element nodes are given as follows:

$$\begin{aligned} P_1 & \begin{cases} \alpha_1 = 0, \\ \beta_1 = 0, \end{cases} \\ P_2 & \begin{cases} \alpha_2 = \|\vec{\alpha}\|, \\ \beta_2 = 0, \end{cases} \\ P_3 & \begin{cases} \alpha_3 = \frac{|\overrightarrow{P_1 P_2} \cdot \overrightarrow{P_1 P_3}|}{\|\overrightarrow{P_1 P_2}\|}, \\ \beta_3 = \|\vec{\beta}\|. \end{cases} \end{aligned} \quad (B.12)$$

Coordinates of the nodal displacement field. The coordinates of the nodal displacement field are given as follows:

$$\begin{aligned} p_i &= \begin{bmatrix} u_i \\ v_i \\ w_i \end{bmatrix} [x_{\hat{\alpha}} \quad y_{\hat{\alpha}} \quad z_{\hat{\alpha}}], \\ q_i &= \begin{bmatrix} u_i \\ v_i \\ w_i \end{bmatrix} [x_{\hat{\beta}} \quad y_{\hat{\beta}} \quad z_{\hat{\beta}}]. \end{aligned} \quad (B.13)$$

Real-world coordinates of the resulting nodal forces. The real-world coordinates of the resulting nodal forces are given by

$$\begin{bmatrix} x_{Fi} \\ y_{Fi} \\ z_{Fi} \end{bmatrix} = \begin{bmatrix} x_{\hat{\alpha}} & x_{\hat{\beta}} \\ y_{\hat{\alpha}} & y_{\hat{\beta}} \\ z_{\hat{\alpha}} & z_{\hat{\beta}} \end{bmatrix} \begin{bmatrix} \alpha_{Fi} \\ \beta_{Fi} \end{bmatrix}. \quad (B.14)$$

Appendix C. Silicon phantom construction

The geometry of the deformable phantom consists of a rectangular box ($84 \times 82 \times 70$ mm) containing a rectangular

inclusion ($20 \times 23 \times 20$ mm), which is 4.3 times stiffer than the surrounding silicon (Fig. 5). The gel system is composed of two parts, catalyst (part A), and resin (part B), the ratio of which determines its elastic properties (a decrease in A:B produces stiffer gels). The components, the catalyst (part A) and the resin (part B), both contain silicon copolymers which form cross-links when combined. Since only approximately 2% of the material becomes cross-linked, the material becomes a gel, and its stiffness is directly proportional to the amount of cross-linking (Goldstein et al., 1987). Parts A and B of the gel system were mixed in a ratio 1:1.7. This provided a good combination of flexibility under compression and integrity under gravity, for the surrounding silicon in the phantom. Parts A and B of the gel system were then mixed in a ratio 1:5.7, for the stiff inclusion. The phantom was built as follows:

1. The molds consist of two rectangular boxes, one of size ($84 \times 82 \times 70$ mm) to house the whole silicon phantom, and another smaller mold of size ($20 \times 23 \times 20$ mm) used to make the stiff silicon inclusion. Both molds are made of heat-resistant PVC. The inside walls of the molds were sprayed with Palm oil, and covered with sheets of transparent plastic wrapper, making it much easier to remove the silicon phantoms out of the molds when ready.
2. Parts A and B of the gel system were mixed in a ratio 1:1.7. This provided a good combination of flexibility under compression and integrity under gravity. The mix was stirred for 5 minutes, and then poured into the larger mold so as to fill about half of the mold.
3. Parts A and B of the gel system were then mixed in a ratio 1:5.7, stirred for 5 minutes and then poured into the smaller mold in order to fill it up.
4. Both molds were then heated up at 175°F for 36 h, the time needed for the gel systems to cure. The heat acted as a catalyst in the curing process.
5. The stiff silicon gel inclusion was removed from its mold, and then placed inside the larger mold on the top of the already cured silicon gel.
6. Parts A and B of the gel system were again mixed in a ratio 1:1.7, stirred for 5 minutes and then carefully poured into the larger mold in order to fill it up.
7. The large mold was heated up again at 175°F during 36 h.
8. The full silicon gel phantom was finally removed from its mold by pulling on the plastic wrap paper, and secured inside a custom-built pressure device (also made of PVC material, which does not cause any extraneous signal when imaged in the MR machine).

References

- ABAQUS/Standard V.5.8, 1998. Hibbitt, Karlsson and Sorensen. Vol. II, 14.1.4–1, 14.1.4–17.
- Agache, P.G., Monneur, C., Leveque, J.L., DeRigal, J., 1980. Mechanical properties and Young's modulus of human skin in vivo. *Arch. Dermatol. Res.* 269, 221–232.
- Azar, F.S., Metaxas, D., Schnall, M.D., 1999. A finite element model of the breast for predicting mechanical deformations during interventional procedures. *Proc. Int. Soc. Magn. Reson. Med.* 7, 1084.
- Azar, F.S., Metaxas, D.N., Miller, R.T., Schnall, M.D., 2000. Methods for predicting mechanical deformations in the breast during clinical breast biopsy. In: 26th IEEE Annual N.E. BioEngineering Conference.
- Azar F.S., Metaxas D.N., Schnall M.D., 2001. A deformable finite element model of the breast for predicting mechanical deformations under external perturbations. *J. Acad. Radiol.* October issue.
- Baumann, R., Glauser, D., 1996. Force feedback for virtual reality based minimally invasive surgery simulator. In: *Medicine Meets Virtual Reality*. IOS Press, Amsterdam.
- Behrenbruch, C.P., Marias, K., Armitage, P., Yam, M., Moore, N., English, R.E., Brady, M., 2000. MRI-mammography 2D/3D data fusion for breast pathology assessment. In: *Proc. Medical Image Computing and Computer Assisted Intervention (MICCAI)*, pp. 307–316.
- Carvalho, B.M., Gau, C.J., Herman, C.T., Kong, T.Y., 1999. Algorithms for fuzzy segmentation. *Pattern Anal. Appl.* 2, 73–81.
- Chadwick, J., Haumann, D., Parent, R., 1989. Layered construction of deformable animated characters. *Computer Graphics (SIGGRAPH'89)* 23, 243–252.
- Chen, D.T., Zeltzer, D., 1992. Pump it up: computer animation of a biomechanically based model of the muscle using the finite element method. *Computer Graphics (SIGGRAPH'92)* 26, 89–98.
- Cook, R.D., Malkus, D.S., Plesha, M.E., 1989. In: *Concepts and Applications of Finite Elements Analysis*. Wiley, New York.
- Cotin, S., Delinguet, H., Ayache, N., 1999. Real-time elastic deformations of soft tissues for surgery simulation. *IEEE Trans. Visualization Computer Graphics* 5, 62–73.
- Desbrun, M., Gascuel, M.P., 1995. Animating soft substances with implicit surfaces. *Computer Graphics (SIGGRAPH'95)* 287–290.
- DeVries, P.L., 1994. In: *A First Course in Computational Physics*. Wiley, New York, pp. 207–225.
- Egan, R.L., 1988a. Breast Embryology, Anatomy and Physiology. *Breast Imaging: Diagnosis and Morphology of Breast Diseases*. Saunders. pp. 30–58.
- Egan, R.L., 1988b. Malignant Breast Lesions. *Breast Imaging: Diagnosis and Morphology of Breast Diseases*. Saunders. pp. 227–231.
- Elden, H.R., 1977. In: *Biophysical Properties of Skin*. Wiley-Interscience, New York.
- Ergatoudis, I., Irons, B.M., Zienkiewicz, O.C., 1968. Curved isoparametric, 'quadrilateral' elements for finite element analysis. *Int. J. Solids Structures* 4, 31–42.
- Fischer, U., Vosschenrich, R., Keating, D., Bruhn, H., Doler, W., Oestmann, J.W., Grabbe, E., 1994. MR-guided biopsy of suspect breast lesions with a simple stereotaxic add-on device for surface coils. *Radiology* 192, 272–273.
- Fischer, U., Vosschenrich, R., Doler, W., Hamadeh, A., Oestmann, J.W., Grabbe, E., 1995. MR imaging-guided breast intervention: experience with two systems. *Radiology* 195, 533–538.
- Fung, Y.C., 1972. Stress-strain history relations of soft tissues in simple elongation. In: Fung, Y.C., Perrone, N., Anliker, M. (Eds.), *Biomechanics: Its Foundations and Objectives*. Prentice-Hall, Englewood Cliffs, NJ.
- Fung, Y.C., 1981. In: *Biomechanics: Mechanical Properties of Living Tissues*. Springer, New York, pp. 203–212.
- Fung, Y.C., 1993. In: *Biomechanics: Mechanical Properties of Living Tissues*, 2nd Edition. Springer, New York.
- Fung, Y.C., 1994. In: *A First Course in Continuum Mechanics*. Prentice Hall, Englewood Cliffs, NJ.
- Goldstein, D.C., Kundel, H.L., Daube-Whiterspoon, M.E., Thibault, L.E., Goldstein, E.J., 1987. A silicone gel phantom suitable for multimodality imaging. *Invest. Radiol.* 22, 153–157.

- Green, A.E., Zerna, W., 1968. In: *Theoretical Elasticity*. Oxford University 99, London.
- Haber, I., Metaxas, D., Axel, L., 2000. Three-dimensional motion reconstruction and analysis of the right ventricle using tagged MRI. *Medical Image Analysis* 4, 335–355.
- Harris, J.R., Lippman, M.E., Morrow, M., Hellman, S., 1996. In: *Diseases of the Breast*. Lippincott-Raven, New York.
- Hayes, W.C., Keer, L.M., Hermann, G., Mockros, L.F., 1972. A mathematical analysis for indentation tests of articular cartilage. *J. Biomech.* 5, 541–551.
- Joukhadar, A., 1995. Energy based adaptive time step and inertia-matrix based adaptive discretization for fast converging dynamic simulation. In: *Proc. of the Int. Workshop on Visualisation and Mathematics*. Springer, Heidelberg.
- Kojic, M., Bathe, K.J., 1987. Studies of finite element procedures-stress solution of a closed elastic strain path with stretching and shearing using the updated Lagrangian Jaumann formulation. *Computers Structures* 26, 175–179.
- Krouskop, T.A., Wheeler, T.M., Kallel, F., Garra, B.S., Hall, T., 1998. The elastic moduli of breast and prostate tissues under compression. *Ultrasonic Imaging* 20, 151–159.
- Kuehnafel, U.G., Neisius, B., 1993. CAD-based graphical computer simulation in endoscopic surgery. *Endosc. Surg.* 1, 181–184.
- Lawrence, A.J., Rossman, P.J., Mahowald, J.L., Manduca, A., Hartmann, L.C., Ehman, R.L., 1999. Assessment of breast cancer by magnetic resonance elastography. *Proc. Int. Soc. Magn. Reson. Med.* 7, 525.
- Luciani, A., Jimenez, S., Florens, J.L., Cadoz, C., Raoult, O., 1991. Computational physics: a modeler simulator for animated physical objects. In: *Eurographics Workshop on Animation and Simulation*, pp. 425–437.
- Maurel, W., Wu, Y., Magnenat Thalmann, N., Thalmann, D., 1998. *Biomechanical Models for Soft Tissue Simulation*. Basis Research Series. Esprit. Springer, Berlin.
- Meseure, P., Chaillou, C., 1997. Deformable body simulation with adaptive subdivision and cuttings. In: *Proceedings of the Fifth International Conference in Central Europe on Computer Graphics and Visualization*. Pergamon, Oxford, pp. 361–370.
- Metaxas, D., 1992. Physics-based modeling of nonrigid objects for vision and graphics. Ph.D. thesis, Department of Computer Science, University of Toronto.
- Metaxas, D., Terzopoulos, D., 1993. Shape and nonrigid motion estimation through physics-based synthesis. *IEEE Trans. Pattern Anal. Machine Intelligence* 15, 569–579.
- Miller, G., 1988. The motion dynamics of snake and worms. *Computer Graphics (SIGGRAPH'88)* 23, 169–173.
- NCI, 1998. *Understanding Breast Cancer Treatment*. National Cancer Institute. NIH 98-4251, 6-7.
- Norton, A., Turk, G., Bacon, B., Gerth, J., Sweeney, P., 1991. Animation of fracture by physical modeling. *The Visual Computer* 7, 210–219.
- Orel, S.G., Schnall, M.D., Newman, R.W., Powell, C.M., Torosian, M.H., Rosato, E.F., 1994. MR imaging-guided localization and biopsy of breast lesions: initial experience. *Radiology* 193, 97–102.
- Park, J., Metaxas, D., Young, A.A., Axel, L., 1996a. Analysis of left ventricular wall motion based on volumetric deformable models and MRI-SPAMM. *Med. Image Anal.* 1, 53–71.
- Park, J., Metaxas, D., Young, A.A., Axel, L., 1996b. Deformable models with parameter functions for cardiac motion analysis from tagged MRI data. *IEEE Trans. Medical Image Processing* 15 (3), 278–289.
- Picinbono, G., Delinguet, H., Ayache, N., May 2001. Non-linear and anisotropic elastic soft tissue models for medical simulation. In *ICRA2001: IEEE International Conference on Robotics and Automation*, Seoul, South Korea.
- Press, W.H., Teukolsky, S.A., Vetterling, W.T., Flannery, B.P., 1992. In: *Numerical Recipes in C: The Art of Scientific Computing*. Cambridge University Press, Cambridge, pp. 707–725.
- Reddy, N.P., Song, G.J., 1995. Tissue cutting in virtual environments. *Medicine meets virtual reality IV*. In: *Interactive Technology and the New Paradigm for Healthcare*. IOP Press, Amsterdam, pp. 359–364.
- Saha, P.K., Udupa, J.K., Odhner, D., 2000. Scale-based fuzzy connected image segmentation: theory algorithms, and validation. *Computer Vision and Image Understanding* 77, 145–174.
- Sarvazyan, A.P., Skovoroda, A.R., Emelianov, S.Y., Fowlkes, J.B., Pippi, J.G., Adler, R.S., Buxton, R.B., Carson, P.L., 1995. In: *Biophysical Bases of Elasticity Imaging*. Plenum, New York.
- Schneider, D.C., Davidson, T.M., Nahum, A.M., 1984. In vitro biaxial stress-strain response of human skin. *Arch. Otolaryngol.* 110, 329–333.
- Sciaretta, J., Bishop, J., Samani, A., Plewes, D.B., 1999. MR validation of soft tissue deformation as modeled by non-linear finite element analysis. *Proc. Int. Magn. Reson. Med.* 7, 246.
- Skovoroda, A.R., Gusakyan, D.A., Mayevskii, Y.I., Yermilova, V.D., Oranskaya, G.A., Sarvazyan, A.P., 1995. Quantitative analysis of the mechanical characteristics of pathologically changed soft biological tissues. *Biophysics* 40, 1359–1364.
- Speeter, T.H., 1992. Three dimensional finite element analysis of elastic continua for tactile sensing. *Int. J. Robotics Res.* 11 (1), 1–19.
- Spencer, A.J.M., 1980. In: *Continuum Mechanics*. Longman, London, pp. 153–163.
- Stavros, A.T., Rapp, C.L., Dennis, M.A., Parker, S.H., Sisney, G.A., 1995. Solid breast nodules: use of sonography to distinguish between benign and malignant lesions. *Radiology* 196, 123–134.
- Szekely, G., Brechbuhler, Ch., Hutter, R., Rhomberg, A., Schmid, P., 1998. Modelling of soft tissue deformation for laparoscopic surgery simulation. In: *Medical Image Computing and Computer-Assisted Intervention (MICCAI)*, pp. 550–561.
- Veronda, D.R., Westmann, R.A., 1970. Mechanical characterization of skin-finite deformations. *J. Biomech.* 3, 111–124.
- Wellman, P.S., 1999. *Tactile Imaging*. Thesis. Harvard University, Cambridge, MA.
- Wellman, P.S., Howe, R.D., 1998. *Harvard Bio-Robotics Lab.Tech. Report. #98-121*.
- Williams, C., Clymer, B., Schmalbrock, P., 1999. Biomechanics of breast tissue: preliminary study of force-deformation relationship. *Proc. Int. Soc. Magn. Reson. Med.* 7, 524.
- Young, A.A., Axel, L., Dougherty, L., Bogen, D.K., Parenteau, C.S., 1993. Validation of tagging with MR imaging to estimate material deformation. *Radiology* 188, 101–108.
- Zhang, M., Zheng, Y.P., Mak, A.F., 1997. Estimating the effective Young's modulus of soft tissues from indentation tests — nonlinear finite element analysis of effects of friction and large deformation. *Med. Eng. Phys.* 19, 512–517.
- Zhuang, Y., Canny, J., 1999. Real-time and physically realistic simulation of global deformation. *SIGGRAPH Sketches and Applications*. Los Angeles, CA, 1999.
- Zienkiewicz, O.C., 1977. *The Finite Element Method*, 3rd Edition. McGraw-Hill, London.
- Zienkiewicz, O.C., Taylor, R.L., 1989. *The Finite Element Method*. McGraw-Hill, New York.